



LUND
UNIVERSITY

Master of Science Thesis
HT2020

Material decomposition using a photon counting X-ray detector in low energy range

Rasmus Solem

Supervisors

Martin Bech and Till Dreier

Medical Radiation Physics, Lund
Faculty of Science
Lund University
www.msf.lu.se

Abstract

Material decomposition in X-ray imaging is used to separate different materials or elements in an image and to quantify their respective concentration. The material decomposition and quantification are made possible by the dependency of attenuation on the attenuating material and photon energy. The purpose of this thesis was to implement a material decomposition method, from the image acquisition using a photon counting detector in a laboratory setup to the actual material decomposition, for both radiography and computed tomography. The detector has a 450 μm silicon sensor with 1030×514 square pixels of 75 μm and two configurable energy thresholds. Due to the sensor material and thickness, the detectors quantum efficiency decreases rapidly after 10 keV limiting the photon detection to a low energy X-ray range.

Energy thresholds were set in the range of 4 to 10.5 keV to acquire two images with specific photon energy windows on each side of an absorption edge of a selected element in the sample. The material decomposition was then performed in the image domain based on these images and three separate material images were created with pixel values representing the material fraction in the pixel.

Two samples were used to verify the method, one with copper and silver grids and PMMA and one with a copper cable and aluminium foil for the radiography and computed tomography decompositions respectively. MultiHance, a gadolinium based contrast agent, was diluted with water to five different concentrations to study the concentration quantification for both radiography and computed tomography. Finally, a piece of an atherosclerotic carotid plaque, containing calcium and iron in soft tissue embedded in paraffin wax, was decomposed to test the method on a biological sample.

The verification samples, where the impact of the copper K-edge on the attenuation was clear, decompose well with the exception of regions affected by ring artifacts and beam hardening. The ring artifact arises due to an insufficient amount of photons in the small energy windows and beam hardening is because of highly attenuating materials like copper and thick samples. These artifacts impacted the decomposition of all samples but can hardly be avoided in the current setup. The measured concentrations in the MultiHance samples were in reasonable agreement with the expected concentrations. The gadolinium L-edges had no measurable effect on the attenuation due to too high attenuation in the water in the solution and the PMMA holder that the solutions were filled in. For the plaque sample, iron, calcium and paraffin were decomposed with a reasonable distribution of the materials in the plaque.

The materials suited for decomposition and the thickness of the samples are limited by the low energy range, but the method could be verified. The concentration quantification of the MultiHance samples were mainly achieved by the large difference in the attenuation value between the materials in the sample. But as the general method works for samples containing materials with visible absorption edges, it is reasonable to assume that the concentration quantification would yield accurate results for samples with materials of similar attenuation but with one visible absorption edge.

Populärvetenskaplig sammanfattning

Fotoner som penetrerar ett material har olika sannolikheter att växelverka och därmed överföra sin energi och absorberas i materialet eller få en riktningsförändring. Denna sannolikhet för fotonen att absorberas eller spridas anges ofta per längdenhet och kallas för attenuering. Sannolikheten för attenuering i ett material ökar med sjunkande fotonenergi och om materialet består av ett högre atomnummer och högre densitet samt ju tjockare materialet är. I vanliga röntgenbilder är det denna skillnad i attenuering mellan material som gör det möjligt att särskilja olika material så som ben och mjukvävnad där ben har en högre attenuering. Ett fenomen kallat absorptionskanter leder till att attenueringen ökar drastiskt vid vissa energier som beror på bindningsenergi för elektroner i atomens elektronskal. Dessa absorptionskanter är således materialspecifika. Idén med materialuppdelade röntgenbilder är att kunna särskilja olika material med liknande attenuering i ett objekt. Fotonerna som används för att skapa en röntgenbild genererar ett spektrum av energier och att attenueringen är beroende av fotonernas energi utnyttjas för att utföra materialuppdelningen.

Redan på 1970-talet implementerades metoder för materialuppdelning som bygger på att två olika insamlingar görs, en med fotoner med låg energi och en med fotoner med högre energi, med så kallad "dual-energy" teknik. Detta har vidareutvecklats och används både i kliniska undersökningar och forskning. Olika metoder används för att samla in "dual-energy" data och på senare år så har nya så kallade fotonräknande detektorer implementerats för detta. Dessa detektorer bygger på halvledarmaterial, som är ett mellanting mellan ledare och isolatorer, där fotonerna växelverkar vilket leder till att en elektrisk signal skapas som kan läsas ut. Denna signal är proportionerlig mot den inkommande fotonens energi och kan således jämföras mot en förinställd tröskelenergi. Om fotonens energi är lika stor eller större än tröskelenergin så räknas fotonen. Med hjälp av två tröskelenergi kan således ett energifönster skapas där endast fotoner inom ett visst energiintervall räknas.

I detta arbete används en sådan detektor för att implementera en metod för materialuppdelning och koncentrationskvantifiering i en laborativ röntgenuppställning för fotoner i ett lågenergiområde, eftersom detektorn som används snabbt blir ineffektiv för fotoner med energier över 10 keV. Metoden skulle fungera både för slätröntgen och dator-tomografiska rekonstruktioner. En fungerande materialuppdelning kan sedan implementeras som en metod för att lokalisera intressanta områden för vidare undersökningar på synkrotronanläggningar. En materialuppdelningsmetod som bygger på två bilder insamlade med olika energinivåer användes.

Olika fantom skapades för att verifiera att metoden fungerade för både slätröntgen och datortomografi, dessa innehöll koppar vilket har en absorptionskant inom det detekterbara energiintervallet samt ett eller två ytterligare material med liknande attenuering men utan absorptionskanter. Fantom med rör som fylldes med olika koncentrationer av ett gadoliniumbaserat kontrastmedel skapades för att undersöka möjligheten att kvantifiera materialkoncentrationer. Slutligen användes metoden för att dela upp järn, kalcium och mjukvävnad i ett aterosklerosplackprov.

Resultaten från materialuppdelningen av de olika fantomen visar på att den implementerade metoden fungerar men att fotonernas låga energier medför begränsningar på möjliga material och provens tjocklek. Materialuppdelningen av de datortomografiska rekonstruktionerna påverkas av artefakter i bilderna som är svåra att undvika i uppställningen. Kvantifieringen av olika koncentrationer har en relativt god överenskommelse med de faktiska koncentrationerna och uppdelningen i det biomedicinska plackprovet har en rimlig fördelning av materialen. Metoden är dock beroende av förkunskap om materialen i proven samt på val som görs utav operatören av uppdelningen.

Contents

1	Introduction	1
1.1	Aim	1
2	Theory	2
2.1	X-ray attenuation	2
2.2	Photon counting detector	3
2.2.1	Sensor material	3
2.2.2	Signal readout	5
2.2.3	Quantum efficiency	6
2.2.4	Image artifacts	6
2.3	Material decomposition	6
2.3.1	Post-image reconstruction material decomposition	7
2.3.2	Pre-image reconstruction material decomposition	7
3	Materials and methods	8
3.1	Decomposition samples	8
3.1.1	Copper and silver grids	8
3.1.2	Copper cable and aluminium foil	9
3.1.3	MultiHance concentrations	9
3.1.4	Atherosclerotic plaque	10
3.2	Image acquisition	11
3.2.1	Detector parameters	12
3.2.2	Image corrections	12
3.2.3	Energy window selection	12
3.2.4	CT reconstruction	12
3.3	Material decomposition	13
3.3.1	Decomposition attenuation value selection and correction	13
4	Results	14
4.1	Copper and silver grids sample	15
4.2	Copper cable and aluminium foil sample	17
4.3	MultiHance samples	19
4.3.1	Radiography	20
4.3.2	Computed tomography	21
4.3.3	Energy spectrum	24
4.4	Atherosclerotic plaque sample	25
4.4.1	Verification of multiple materials in calcification	26
5	Discussion	29
5.1	MultiHance contrast agent sample	30
5.2	Atherosclerotic plaque sample	30
6	Conclusions	32
7	Acknowledgements	33
8	References	34
A	Appendix	36

1 Introduction

Regular X-ray images display the attenuation differences between materials in the imaged object. Thus showing good contrast between hard and soft materials like bone and soft tissue, whereas materials with similar attenuation can hardly be distinguished. The idea of doing a material decomposition to separate different materials and elements is based on the attenuation's material and energy dependence, i.e. that different elements show different attenuation properties for different photon energies. Therefore, acquiring images with different photon energies provides the information necessary to differentiate materials in an object.

In 1976 Alvares and Macovski showed that material specific constants that determines photoelectric and Compton scattering interactions in a sample could be calculated from dual-energy measurements [1]. They constructed basis functions based on the photoelectric and Compton scatter interaction dependencies of the elements atomic number and electron density respectively. With these basis functions and dual-energy measurements, effective atomic number and electron density of the material could be calculated [2; 3]. With their groundwork, different methods for material decomposition has been created both for clinical and pre-clinical use, mainly for computed tomography (CT) data.

The acquisition of images with different photon energies can be accomplished in multiple ways. With integrating detectors for dual-energy computed tomography (DECT) acquisitions it is usually done either with a single source, dual source or dual-detector based system [4; 2]. Single source systems use one X-ray-tube where the tube voltage switches between a high and low voltage to obtain the DECT. Dual source systems use two X-ray tubes with separate detectors and different tube voltages. The detector based system is a single source system but the detector consists of two detector layers, with the first layer detecting low energy photons and the second layer detecting photons with higher energies. With the development of photon counting detectors, primarily for pre-clinical systems but lately also in clinical prototypes, new ways of acquiring dual-energy data are enabled [2; 5]. As these detectors count each photon and measure its individual energy, the detected photons can be placed in separate energy bins providing the energy dependent information necessary for material decomposition with a single source and one tube voltage. With the energy information in the data, the material decomposition is either performed pre- or post-reconstruction or as a mix of the two [2]. In this thesis, the post-reconstruction decomposition is used because of its simplicity.

1.1 Aim

Due to the used 450 μm silicon (Si) sensor, the detectors quantum efficiency decreases rapidly above 10 keV limiting the photon detection to a low energy X-ray range.

The aim of this thesis is to implement a material decomposition method in a low energy X-ray laboratory set up with a photon counting detector, to differentiate and quantify the concentration of different materials and elements in a sample. This includes the acquisition of the X-ray images as well as the actual material decomposition for both radiography and CT. The post-reconstruction decomposition is based on two separate energy windows resulting in three individual material images.

The material decomposition could be an initial part of the research chain for samples like atherosclerotic carotid plaque, to identify regions of calcium and iron before further measurements, for instance X-ray fluorescence at a synchrotron facility, are carried out.

2 Theory

2.1 X-ray attenuation

The amount of photons transmitted through an object depends on the linear attenuation coefficient μ , which is the probability per unit length for a photon to interact with a material. The linear attenuation coefficient is a summation of the contributions from different types of interactions. Regarding photon interaction with matter, the three major interaction types where photon energy is transferred to electrons in the absorbing material are the photoelectric absorption, Compton scattering (incoherent) and pair production. In the energy range for standard X-ray imaging pair production is not possible as the photon energies are significantly below 1.022 MeV. The detected photon energies in this project ranges from 4 - 11 keV which makes the photoelectric absorption the dominant interaction process but it also leads to coherent scattering contributing to the attenuation coefficient [6].

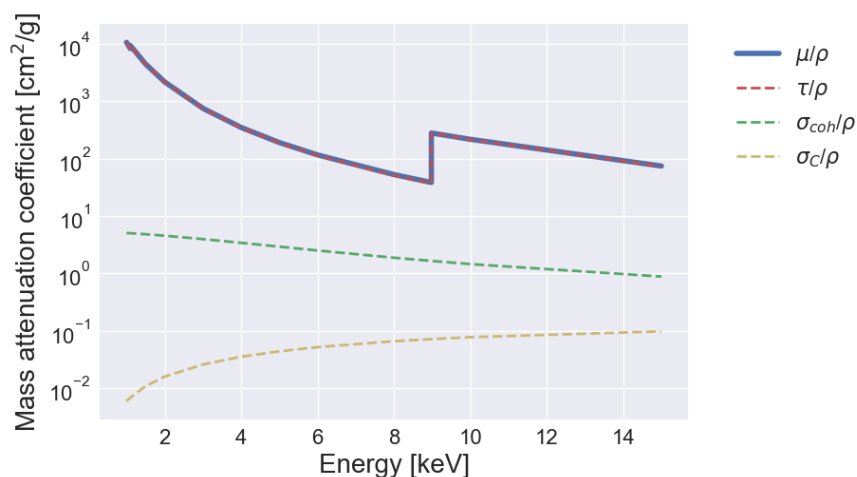


Figure 1: The total mass attenuation coefficient, μ/ρ , for copper and the contribution from the three, for this project, relevant interaction processes: photoelectric absorption, coherent scattering and Compton scattering, τ/ρ , σ_{coh}/ρ and σ_C/ρ respectively. The effect of the copper K-edge is visible at 9 keV. Attenuation data from XCOM [7].

Photoelectric absorption, τ , is the process of the photon transferring all its energy and therefore disappears and a photoelectron is then emitted from the atom leaving a vacancy in the atomic shell. The photoelectron is emitted with a kinetic energy that is equal to the difference between the photon energy and the electron binding energy. If the photon energy is sufficiently high, the photoelectron is most likely to be emitted from the innermost K-shell [8]. The vacancy in the atomic shell is thereafter filled by an electron from an outer shell resulting in the emission of either characteristic X-rays with the energy equalling the difference in binding energy between the shells or an Auger electron.

With the exception of absorption edges, the photoelectric contribution to the attenuation coefficient decreases with increasing energy as seen in Figure 1. When the photon energy reaches the energy of an absorption edge, relating to the electron binding energies of the atomic shells, the probability for photoelectric absorption drastically increases as it is then possible to eject more electrons from the atom. The photoelectric absorption is also element dependent and is more likely for elements with a higher atomic number Z . An approximation of the probability for photoelectric absorption is

$$\tau \approx constant \cdot \frac{Z^n}{E_\gamma^{3.5}} \quad (1)$$

where n differs between 4 and 5 depending on the photon energy E_γ [8].

As seen in Figure 1, coherent scattering σ_{coh} and Compton scattering σ_C only contribute with a small part to the total attenuation in this energy interval. When coherent scattering occurs, the photon interacts with the bound electrons without ionizing or exciting the atom and the photon path slightly changes direction but with a negligible energy loss. The probability for coherent scattering is higher for low energy photons interacting with atoms with a high atomic number since there are more electrons interfering with the photon. Compton scattering on the other hand, results in a scattered photon and a recoil electron. The incident photon transfers some of its energy to an electron that is then emitted with a kinetic energy that equals the difference between the incident and scattered photons energies. The scattered photons energy is dependent of the incident photon energy and the scattering angle. For low energy incident photons, the scattered photon has almost the same probability for forward and backscattering but with increasing photon energy, the forward scattering is dominant. The probability for Compton scattering increases linearly with the atomic number since there are more electrons to interact with [8]. In the energy range displayed in Figure 1 the probability for Compton scattering increases with increasing energy.

For a photon beam with the initial intensity I_0 , the beam intensity I , after it has passed a distance d through an object with the total attenuation μ , can be written as

$$I = I_0 e^{-\mu d}. \quad (2)$$

2.2 Photon counting detector

For conventional detectors used for X-ray imaging, an indirect conversion technique is used. These detectors have a scintillating layer converting the incident photons to visible scintillation photons via fluorescence as a result of the incident photons interaction with the material. These scintillation photons are detected and converted to an electric signal in an array of photodiodes. The output signal from a pixel is the integrated signals from all detected photons in that pixel, hence the energy information of the individual photons are lost [9].

The energy integrating detector is still the standard detector in clinics but recently pre-clinical and clinical prototypes of photon counting detector systems have been developed [2; 5; 9]. These detector systems are direct conversion systems where the step of converting the incident photons to scintillating photons is skipped. Instead the active material is a semiconductor where the photons are directly converted into an electrical signal. The conceptual differences between the integrating detectors and photon counting detectors are shown in Figure 2.

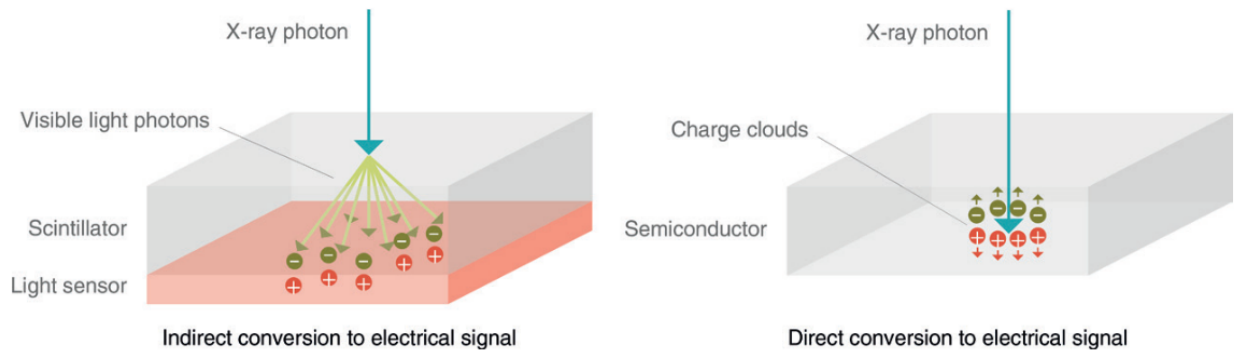


Figure 2: Drawing of the principles of the energy integrating detector to the left and the photon counting detector to the right for one detector element [5].

2.2.1 Sensor material

Silicon and germanium are the most important semiconductor materials [10], but for photon counting detectors materials as cadmium telluride, cadmium zinc telluride and gallium arsenide are also widely used [5; 9; 10]. Cadmium telluride and cadmium zinc telluride detectors are normally constructed with a ohmic contact and have a constant

electric field inside the material. For silicon detectors on the other hand, the detector is made with a pn-junction.

In the silicon crystal, each atom's four valence electrons are shared and create a valence band where the electrons are bound to specific positions within the lattice. At higher electron levels, the electrons can freely move and create the conduction band. The material is determined to be an insulator, semiconductor or a conductor depending on the size of the bandgap between these bands. For an insulator, the bandgap is generally above 5 keV, for semiconductors it is around 1 keV and for conductors the bands are overlapping [8; 10].

If the semiconductor crystal is doped with a low concentration of atoms from group *V* in the periodic table, the material is said to be of n-type. The added impurity of the doping atom which has five valence electrons, results in an extra electron that is not fully bounded in the crystal lattice. These electrons create a donor level just under the conduction band as they are loosely bound and have a high probability to be thermally excited to the conduction band. Therefore, the n-type material has many electrons in the conduction band and few holes in the valence band. On the other hand, if the impurity is from group *III* in the periodic table there would be a vacancy in the crystal bond. An electron filling this vacancy is not as tightly bound as the valence electrons, creating an acceptor level just above the valence band. These acceptor levels are filled by thermally excited electrons from the valence band, hence resulting in many holes in the valence band and few electrons in the conduction band for p-type materials [8; 10].

A p-type and a n-type crystal put together create the pn-junction where the free charges in both crystals drift apart [10]. As electrons in the n-type and holes in the p-type move to the sides, positive and negative space charges are built up in the n-type and p-type sides respectively creating a potential difference over the junction called the depletion region [8] shown in Figure 3. This region can be widened by applying a reverse bias voltage over the crystal. In most cases a completely depleted sensor is used. To achieve this, the reversed bias voltage is set to the so called depletion voltage V_d described by

$$V_d = \frac{eNT^2}{2\epsilon}, \quad (3)$$

where e is the electron charge, N the lower of the two dopant concentrations, T the sensor thickness and ϵ the dielectric constant of the sensor material [8].

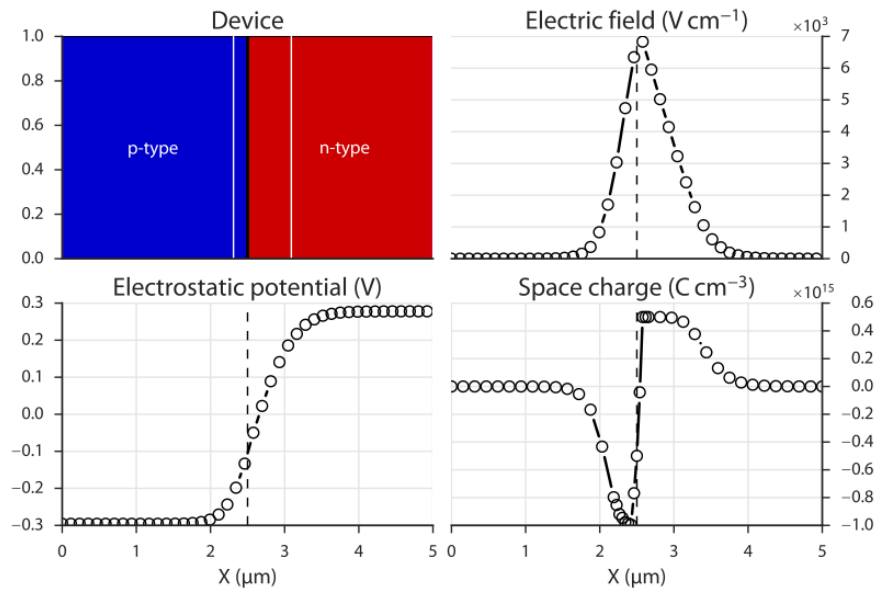


Figure 3: A simulated silicon pn-junction with the depleted region shown between the white lines [10].

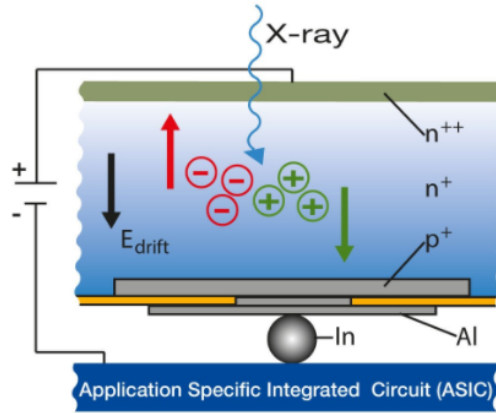


Figure 4: Drawing of a pixel element with the applied high voltage over the sensor and the deposition of energy from an incident photon [11].

2.2.2 Signal readout

Photons incident on the detector interact in the depleted region of the sensor and create a charge cloud as a result of the energy deposition. The charges move in the electric field inducing a current in the pixel electrodes. The current is proportional to the energy deposited in the sensor by the photon [10]. In a hybrid photon counting detector, the sensor is bump bonded to the application specific integrated circuit (ASIC) to connect the sensor pixels to their individual parts of the ASIC. In the ASIC, the signal from each pixel is individually amplified, shaped and digitized. The signal contains information about the photon energy and is compared to a preset global energy threshold that is corrected to each individual pixel to compensate for differences between pixels [12]. If the photon energy exceeds the set energy threshold the photon is counted. Most detectors have two to eight thresholds that can be set to enable the creation of energy bins in addition to eliminating electronic noise [5], as shown in Figure 5. An alternative approach for the measuring of photon energy is time-over-threshold, where the time a pulse from a detected photon is above a set threshold is measured and the time is proportional to the deposited energy [13].

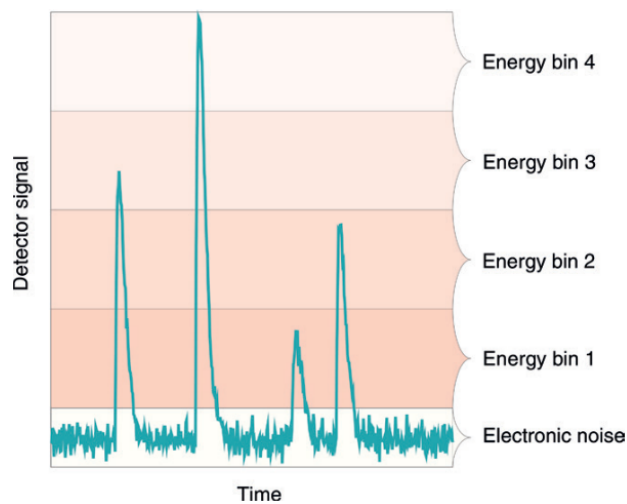


Figure 5: Graph of the energy threshold principle of the photon counting detector [5].

The signal from one photon would in an ideal situation only contribute to a signal in one pixel. The photon may interact through Compton scattering which could result in the deposition of energy in multiple pixels. Photons with

energies higher than the sensor materials K-edge may lead to fluorescence X-rays that could be absorbed in another pixel. There is also the risk of charge sharing where the charge cloud from an interaction in one pixel element may spread to another. All of these effects may result in a photon being registered with incorrect energy or in multiple pixels hence reducing the image quality [5].

2.2.3 Quantum efficiency

The detectors quantum efficiency can be defined as the probability for an incident photon to generate a photoelectron, hence being fully absorbed in the detector material [14]. It is used as a quantity of how well the detector can detect photons of a certain energy. The photon energy, sensor material and thickness and the detector construction all influence the quantum efficiency. A thick sensor of a high atomic number has a higher probability of absorbing the incident photon. For increasing photon energy, the quantum efficiency therefore decreases as the probability of absorption decreases [15]. For low energy photons, the quantum efficiency decreases due to absorption in shielding materials in front of the sensor [14].

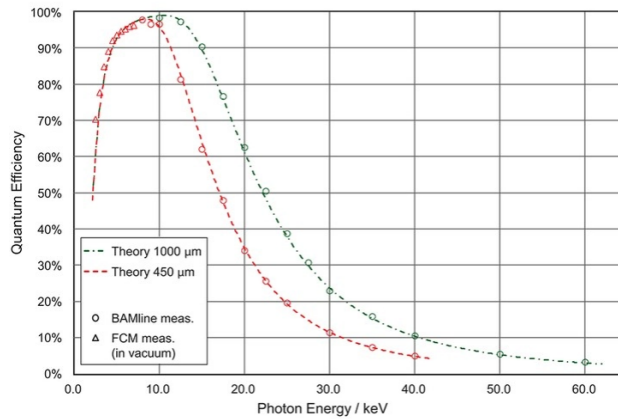


Figure 6: Quantum efficiency measured at the PTB laboratory at BESSY II for two silicon detectors [15].

2.2.4 Image artifacts

In the CT reconstructed slices artifact may occur, the most distinct in this thesis are beam hardening and ring artefacts. Beam hardening occur when the polychromatic beam passes through an object and low energy photons are more highly attenuated resulting in an increase in mean photon energy along the beam path. This can result in a cupping artefact where the edges of a reconstructed object show a higher attenuation than the center, even though it is the same material. It can also cause dark streaks between highly attenuating objects in the slices [16]. Ring artefacts are another reconstruction artefact caused by an insufficient amount of counts in the projections or due to imperfect detector elements [17]. They appear as circles centered at the rotation axis.

2.3 Material decomposition

As described in Section 2.1, the attenuation in an object is dependent of the photon energy and material composition in the object. Material decomposition methods utilizes this dependency to separate different materials and elements in an object. In this project a post-image reconstruction method is implemented as it is a quick and fairly simple method that does not require the same calibrations of energy response and basis functions and computationally heavy optimizations as a pre-image reconstruction method [2; 18]. Two different energy windows are used to decompose an image into three basis materials.

2.3.1 Post-image reconstruction material decomposition

The post-image reconstruction method is based on two images acquired from different intervals of the polychromatic X-ray spectrum. The attenuation coefficient of each image element, pixel or voxel depending on radiography or CT, is described as a linear combination of the volume fraction, f_i , multiplied with the attenuation coefficient, $\mu_{i,E}$, of the different materials, $i = 1, 2, 3$, present in the image volume that has been reconstructed based on the photon energy E [2; 3; 19]. Thus, the attenuation coefficient μ_E for any voxel in one energy window image can be written as

$$f_1 \cdot \mu_{1,E} + f_2 \cdot \mu_{2,E} + f_3 \cdot \mu_{3,E} = \mu_E, \quad (4)$$

where the decomposition attenuation coefficient, $\mu_{i,E}$, for each individual material are values corresponding to a volume containing 100% of the each material respectively [20]. These regions and their attenuation values are identified and selected for both energy windows by the person operating the material decomposition.

With the selected decomposition attenuation values, Equation 4 has three unknowns, f_1 , f_2 and f_3 . Since the method is based on only two energy windows contributing with one equation each, another constituent is necessary to not have an underdetermined system to solve for the three material images. For this, it is assumed that the summation of the three material volume fractions is equal to one. Hence,

$$f_1 + f_2 + f_3 = 1. \quad (5)$$

This combined with the two separate energy window images, a system of equations for each voxel can be written as

$$\begin{aligned} f_1 \cdot \mu_{1,E1} + f_2 \cdot \mu_{2,E1} + f_3 \cdot \mu_{3,E1} &= \mu_{E1} \\ f_1 \cdot \mu_{1,E2} + f_2 \cdot \mu_{2,E2} + f_3 \cdot \mu_{3,E2} &= \mu_{E2} \\ f_1 + f_2 + f_3 &= 1. \end{aligned} \quad (6)$$

The system can then be solved for the three unknown material fractions with matrix multiplication written as

$$\begin{bmatrix} f_1 \\ f_2 \\ f_3 \end{bmatrix} = \begin{bmatrix} \mu_{1,E1} & \mu_{2,E1} & \mu_{3,E1} \\ \mu_{1,E2} & \mu_{2,E2} & \mu_{3,E2} \\ 1 & 1 & 1 \end{bmatrix}^{-1} \cdot \begin{bmatrix} \mu_{E1} \\ \mu_{E2} \\ 1 \end{bmatrix}. \quad (7)$$

Additional a priori knowledge used to calculate the unknown material fractions is that the fractions are positive, thus non-negative values are not allowed. In the presence of an absorption edge for an element in the imaged object, energy windows just below and above the edge are preferred for better separation [18].

2.3.2 Pre-image reconstruction material decomposition

Another well used material decomposition method is a pre-image reconstruction decomposition. This method generally results in a better decomposition than the post-reconstruction as corrections for problems like beam hardening and ring artifacts can be included in the reconstruction which improves the material images [2; 21]. Pre-reconstruction methods either has the starting point in a similar linear combination of attenuation values as the post-reconstruction described with Equation 4 [21; 22] or with the summation of each photon interaction type's contribution to the attenuation coefficient [23; 24]. The pre-reconstruction methods require to be solved via iterative processes and rigorous calibrations and optimizations of non-linear functions [2; 21].

3 Materials and methods

In order to implement the material decomposition method, both a method for the acquisition of energy window images and the scripts for the actual decomposition had to be created. The laboratory set up consisted of a prototype solid anode micro-focus x-ray source from Excillum, a sample holder with 4 degrees of freedom, movable in x, y and z direction and rotatable, and an EIGER2 R 500K detector system from DECTRIS, see Figure 7.

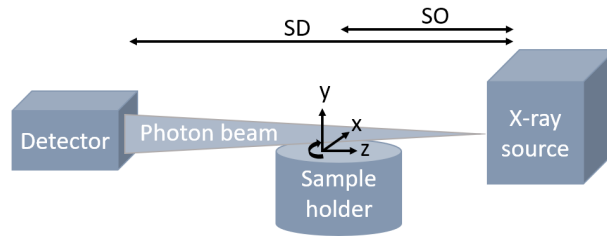


Figure 7: Sketch of the laboratory setup with detector, sample holder and X-ray source. SO = source object distance and SD = source detector distance.

3.1 Decomposition samples

Four different types of samples were used in this thesis. Two were created to verify that the method works and then two to test the capability of it, both for radiography and computed tomography. These are presented below. The possible samples are limited by the laboratory set up. As the detector efficiency decreases rapidly above 10 keV as seen in Figure 6 and energy thresholds can only be set between 4 - 11 keV [25], there are only a few materials with absorption edges within the detectable energy range. The thickness of the sample is also bound by this as there has to be a certain level of transmission through the sample to be able to detect an attenuation difference between the energy windows.

3.1.1 Copper and silver grids

As a verification sample for radiography decomposition, a sample containing copper and silver grids and PMMA was created. Copper has an K-edge at 8.99 keV whereas silver and PMMA have no absorption edges within the energy range. Noteworthy is that the silver grid is most likely a silver alloy as multiple grids had to be stacked to reach an attenuation close to that of copper. As a third material, 4.9 mm of PMMA plastic was added. They were all taped to a card, as seen in Figure 8, that could be placed in the sample holder.

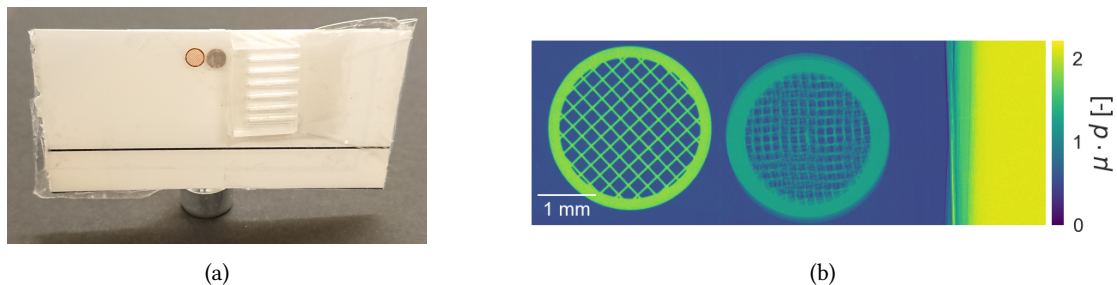


Figure 8: (a) Photography of the copper and silver grids sample and (b) the full spectrum radiography of the sample. The head of the M6 screw visible in (a) is 10 mm for size reference.

During image acquisition, the copper and silver grids sample was placed 10 cm from the source to optimize the field of view for the radiographies. One image and one flat field were taken for each threshold with 30 s exposure time.

3.1.2 Copper cable and aluminium foil

Like the copper and silver grids, this sample was created to verify the decomposition method but for the CT acquisition. Once again copper was used as the material with an absorption edge. A piece of tightly folded aluminium foil was fixated with paraffin wax in the center of a copper cable with the individual copper wires spread out around. The sample was then mounted with paraffin wax to a screw that could be placed in the sample holder.

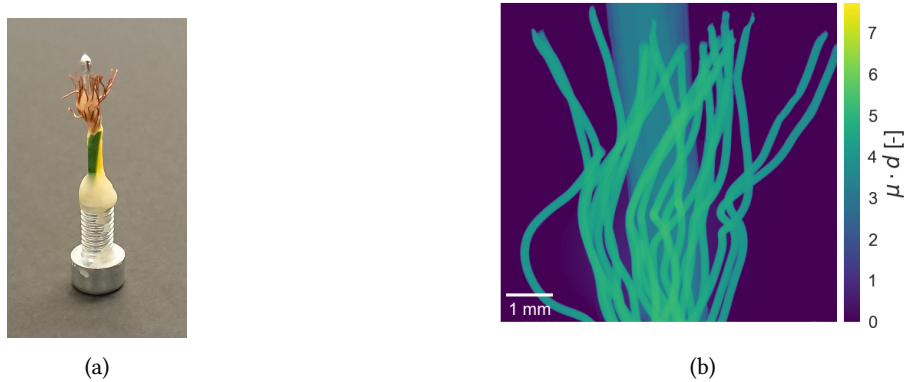


Figure 9: (a) The copper cable and aluminium foil sample mounted with paraffin wax on top of a M6 screw. The head of the M6 screw is 10 mm for size reference. (b) The full energy spectrum radiography of the sample.

During image acquisition, the copper cable and aluminium foil sample was placed 10 cm from the source to optimize the field of view for both radiographies and CT. For radiographies, one image and one flat field were taken for each threshold with 60 s exposure time. 720 projections and 5 flat fields with 100 s exposure time were acquired for each energy window for the CT acquisition.

3.1.3 MultiHance concentrations

To test the decomposition methods capability to quantify the concentration of a material on a volume, the gadolinium contrast agent MultiHance was used as gadolinium has L-edges within the energy range, where the L-III edge at 7.24 keV is the most influential one.

MultiHance is a magnetic resonance imaging contrast agent and the active component in MultiHance is gadobenic acid bound to meglumine as gadobenate dimeglumine. The contrast agent contains 529 mg gadobenate dimeglumine in 1 ml of the fluid [26], resulting in 79 mg of gadolinium per ml. The MultiHance contrast agent was diluted with distilled water volume concentrations of 10, 25, 50, 75 %. Together with the distilled water and the contrast agent on its own, there were six different concentrations of MultiHance ranging from 0 to 100 %.

To hold the MultiHance concentrations, PMMA holders were produced for radiography and CT respectively shown in Figures 10 and 11. Since the goal was to minimize the thickness of the sample, the smallest available drill was used to make holes of 1 mm in diameter in the PMMA. The holes are approximately 1 cm deep. To keep the water in the liquids from evaporating, the holders were sealed with epoxy glue.

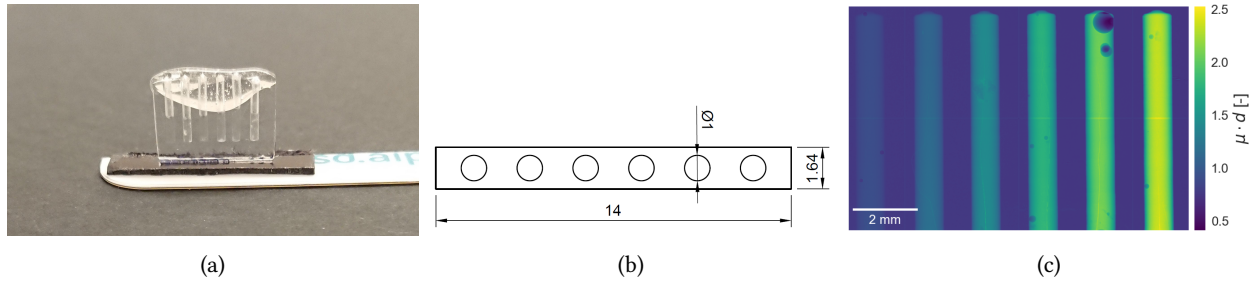


Figure 10: (a) Photography of the MultiHance concentrations holder for radiography acquisition. (b) A schematic drawing of the transverse plane of the holder. The dimensions in the drawing are in mm. (c) A full energy spectrum radiography of the sample with water in the leftmost tube and the MultiHance concentrations from 10 % to 100 % to the right.

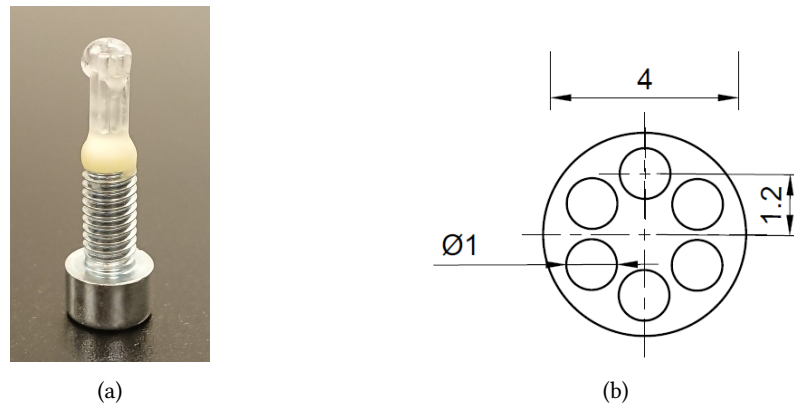


Figure 11: (a) Photography of the MultiHance concentrations holder for CT acquisition mounted on a M6 screw. The head of the screw is 10 mm for size reference. (B) A schematic drawing of the transverse plane of the holder. The dimensions given in the drawing are in mm.

During image acquisition, the MultiHance samples were placed 10 or 15 cm from the source to optimize the field of view for radiographies and CT respectively. For radiographies, one image and one flat field were taken for each threshold with 100 s exposure time. 720 projections and 5 flat fields with 150 s exposure time were acquired for each energy window for the CT acquisition.

In connection to the MultiHance concentrations, a simulated energy spectrum from the source was modified to show the detected spectrum after passing through only MultiHance or also the PMMA holder walls. This was done to see if the gadolinium L-edges' effect on the attenuation were measurable. A simulated energy spectrum was provided by Excillum. The absorption in the silicon sensor and the transmission through the mylar foil covering it were used to simulate the detectors quantum efficiency and the attenuation in 55 cm of air was added to simulate a detected flat field spectrum. The addition of 1 mm MultiHance and 1 mm MultiHance together with 0.64 mm PMMA created the detected spectra. These were also divided by the flat field to create the transmission spectra.

3.1.4 Atherosclerotic plaque

The final sample was a slice of atherosclerotic carotid plaque, shown in Figure 12, which was used to perform a decomposition of a biomedical sample. The plaque contained calcifications which were expected to contain both calcium and iron due to intraplaque hemorrhage. The plaque was embedded in paraffin wax which shows similar attenuation properties to the soft tissue in the plaque. Hence the decomposition was set to decompose iron, calcium

and paraffin wax. The K-edge of iron at 7.11 keV was utilized for the energy window selection. The sample was provided by Isabel Goncalves (CRC Malmö, Skåne University Hospital, Lund University). The local Swedish Ethical Review Authority approved the study (Registration number 472/2005).

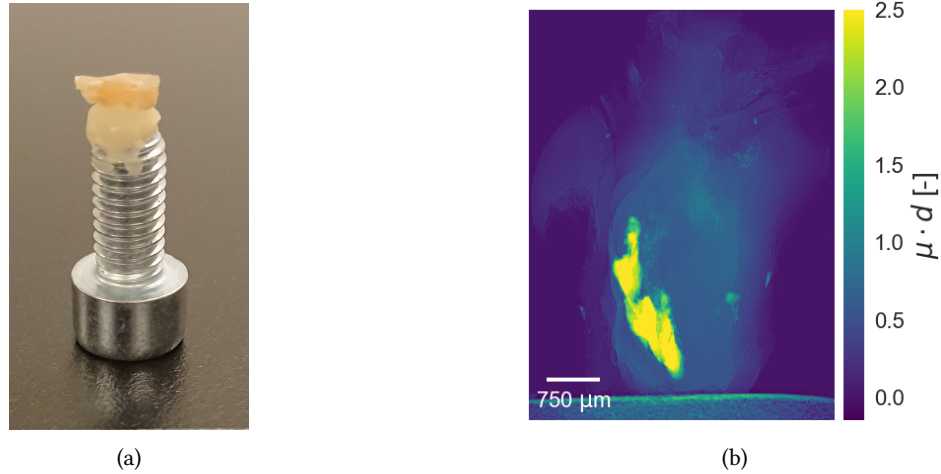


Figure 12: (a) The plaque sample mounted with paraffin wax on top of a M6 screw. The head of the screw is 10 mm for size reference. (b) A full energy spectrum radiography of the sample, here in a standing position.

During image acquisition, the plaque was placed 10 cm from the source to optimize the field of view. For radiographies of the plaque, one image and one flat field were taken for each threshold with 40 s exposure time. 720 projections and 5 flat fields with 45 s exposure time were acquired for each energy window for the CT acquisition.

As the exact content of the plaque sample was unknown an attempt to verify that there was more than one material in the calcification was done. Based on the lower energy window radiography image, the thickness of each pixel if it would only contain calcium was calculated by dividing the pixel value with the tabulated attenuation value [7] of the average energy in the image. With the calculated thickness and the tabulated attenuation value of the average energy in the upper energy window, an upper energy window image was created. This one was compared to the real image and a difference image was calculated. To test this verification method, the same was done for the copper cable and aluminium foil radiographies.

3.2 Image acquisition

For the acquisition, the detector, the motors for the sample holder and the X-ray tube were controlled via Python scripts. Based on pre-existing scripts for the acquisition, new scripts with configurable energy thresholds were created for radiography and CT. For radiographies, one lower energy threshold was set during each acquisition. By the acquisition of multiple images with different set thresholds, energy window images were created by calculating the difference between two energy threshold images. For the CT acquisitions, a differential mode was enabled for the detector where two energy threshold were set and resulting in one energy window image being the difference between the thresholds per acquisition. Hence two acquisitions with different energy thresholds were necessary for a decomposition.

The x-ray source uses a tungsten target and is driven with an acceleration voltage of 70 kV. A 10 μm focal spot is calibrated and internally verified. Images are acquired at 15W emission power. The detector was placed at 55 cm from the X-ray target. Sample position and other image acquisition parameters are presented in each sample's respective section above. The CT acquisitions were done with the sample rotating between the projections that were taken evenly over 360 degrees.

3.2.1 Detector parameters

The detector that was used was an EIGER2 R 500K hybrid single-photon counting detector. The sensor is a reversed-biased silicon diode array that is 450 μm thick. The thickness and material of the detector limits the photon detection to a low energy range as the quantum efficiency decreases rapidly after 10 keV. The sensor module is made of 4×2 readout chips with a total of 1030×514 square pixels of 75 μm . Every pixel has two configurable energy thresholds with two digital counters [12; 25; 27]. The energy resolution of the detector is 1.430 keV FWHM at 8 keV.

3.2.2 Image corrections

Dead and noisy pixels had to be removed from all images and flat fields. The detector has a number of masked pixels that can be easily identified in the image. However, different thresholds might add more under- or over-responsive pixels, which can be identified by a certain deviation from the standard deviation of the image, or by excluding pixels above or below a certain amount of counts. Identified pixels are then replaced by an average value of their respective surrounding pixels obtained using a median filter. This was done with already implemented methods. Energy windows were created by subtracting one threshold image from another, therefore the removing of dead pixels was done again for both images and flat fields.

A flat field correction was done by dividing the image with its corresponding flat field creating transmission images. As the negative natural logarithm of the image values was calculated, pixels with a transmission value over 1 were replaced in the same way as described above to not obtain negative values in the attenuation images.

3.2.3 Energy window selection

The general ambition was to have the energy windows set to each side of the absorption edge of one of the materials in each sample. To get a better decomposition, the width of the windows should be small and separated so that a distinct difference in attenuation between the two images can be obtained. This had to be balanced together with the exposure time and the fact that a wide enough energy window was needed to detect a sufficient amount of photons to generate a good quality image.

To do this, multiple radiographies and corresponding flat fields were acquired with a lower threshold set every 0.5 keV from around 4 keV up to 10 keV depending on the sample. Based on these threshold images, energy window images of widths from 0.5 keV to 3 keV were created by subtracting an image with a higher threshold from an image with a lower threshold. The images were corrected as described in Section 3.2.2, resulting in transmission images. The negative natural logarithm of the pixel values was calculated to obtain the product of the attenuation coefficient and object thickness, $\mu \cdot d$, according to Equation 2. For selected regions of interest (ROIs) that were expected to contain the materials of interest in the samples, these values were then plotted against the energy windows. Error bars representing one standard deviation were added to the measured attenuation coefficients. With the information from these plots and the ambitions for the energy window selection above, the energy windows to implement the material decomposition on were selected.

The energy windows for the CT acquisition of the MultiHance sample were decided based on the MultiHance radiography sample. For the plaque sample, radiographies were acquired before the CT acquisition.

3.2.4 CT reconstruction

Defective pixel values in the projections were corrected as described above and the projections were flat field corrected. The CT reconstruction was done based on the corrected projections with already existing script based on the ASTRA toolbox [28; 29] for MATLAB using cone beam geometry. Center of rotation and tilt correction was performed on the projections. For the MultiHance sample, ring filtering was added using an additive filter as implemented in the HoloTomoToolbox [30].

3.3 Material decomposition

Two energy window images were selected for the decomposition. In the images three regions were selected that represented 100 % of each material. The mean values in the chosen regions were calculated and used for the decomposition attenuation value of each decomposition material. The matrices in Equation 7 were then constructed. To solve the equation for the unknown material fractions, three methods were used and compared.

At first, regular matrix multiplication was done, denoted as F_{matmul} . To put constraints on the material fractions to be between 0 and 1 or just non-negative, two different scipy functions, `scipy.optimize.lsq_linear` and `scipy.optimize.nnls`, were used and denoted as F_{lsq_linear} and F_{nnls} respectively [19]. Both solves a least squares problem using an iterative algorithm to find the best fitted fractions within the bounds. Hence three different results, with three material images each, were calculated for each decomposition sample. The material fractions were calculated pixel by pixel.

To compare the methods, histograms of the material fractions and the sums of fractions in each pixel were created to visualize the difference between the methods.

Regions of interest in the decomposed images were selected and the material fractions in these regions were retrieved. Box plots were created to compare the fractions between the regions, as seen for example in Figure 15. The box displays the data between the upper and lower quartile and the black line showing the median value. The lower whisker marks the lower quartile minus 1.5 times the interquartile range and the upper whisker marks the upper quartile plus 1.5 times the interquartile range. Fractions beyond these values are considered outliers and are shown as rings.

For the MultiHance concentration samples the calculated material fractions in the different tubes were compared to the expected concentrations.

It should be pointed out that for the decomposition of radiography images, the product of the attenuation coefficient and object thickness $\mu \cdot d$ were used as the attenuation coefficients in Equation 7.

3.3.1 Decomposition attenuation value selection and correction

The decomposition attenuation value for the materials are representing 100 % of the specific material. For the verification samples and MultiHance CT sample this was simple selection of regions known to contain only one material. For the plaque sample this was harder. As energy windows were placed on each side of the iron K-edge a region with a large increase in attenuation was selected to represent the iron decomposition attenuation value. As calcium and paraffin have no absorption edge in the energy range, values for these materials were searched for in regions where the attenuation decreased with the higher energy window.

Regarding the MultiHance radiography sample, regions containing MultiHance, water and PMMA were known from the creation of the sample. But as the concentrations were filled in the PMMA holder the images values in the tubes had contributions from both MultiHance or water and PMMA. Since the size of the holder and tubes were known, see Figure 10, a volume through the center of a tube was calculated to contain 39 % PMMA. Hence, 39 % of the PMMA decomposition value was removed from the MultiHance and water values. The MultiHance and water values were then multiplied by the ratio between the holder and tube thicknesses so the decomposition attenuation values corresponded to the full sample thickness containing only MultiHance or water.

4 Results

To calculate the material fractions in the samples, three methods were used as described in Section 3.3. Their differences on the resulting material decomposition are shown in Figure 13, where the decomposition images of the copper and silver grid sample for all three methods are shown as an example. It is clear that for the standard matrix multiplication, F_{matmul} , the fractions are unbounded and spread far below 0 and above 1. As the other two methods put constraints on the fractions, either forcing the fractions to be non-negative when using F_{nnls} , or between 0 and 1, when using $F_{lsq.linear}$ the decomposed images show its respective material much clearer.

With the added constraints for F_{nnls} and $F_{lsq.linear}$ the fractions no longer sum up to 1 for each pixel which is shown in Figure 14. Therefore some pixels contain more or less than 100% material which is reasonable as it is known that the background is just a thin card and consequently pixels in the background should contain less material than those with copper, silver or PMMA.

In Figure 15 the material fractions for regions in each material are shown as box plots. Once again, the different constraints of the three decomposition methods are clear. Noteworthy is that the median fraction for each material region in its respective material image is closest to the true value for the matrix multiplication F_{matmul} .

The resulting material images are clearer for the non-negative constrained F_{nnls} than the matrix multiplication method F_{matmul} . It also allows fractions to be above 1, which could be the case considering that the material value for 100% of each material is chosen manually in regions where is suspected but not known to only be one material but shows no large difference to $F_{lsq.linear}$ when known single material regions are chosen. Therefore, the material decomposed images presented from now on are created with F_{nnls} unless stated otherwise.

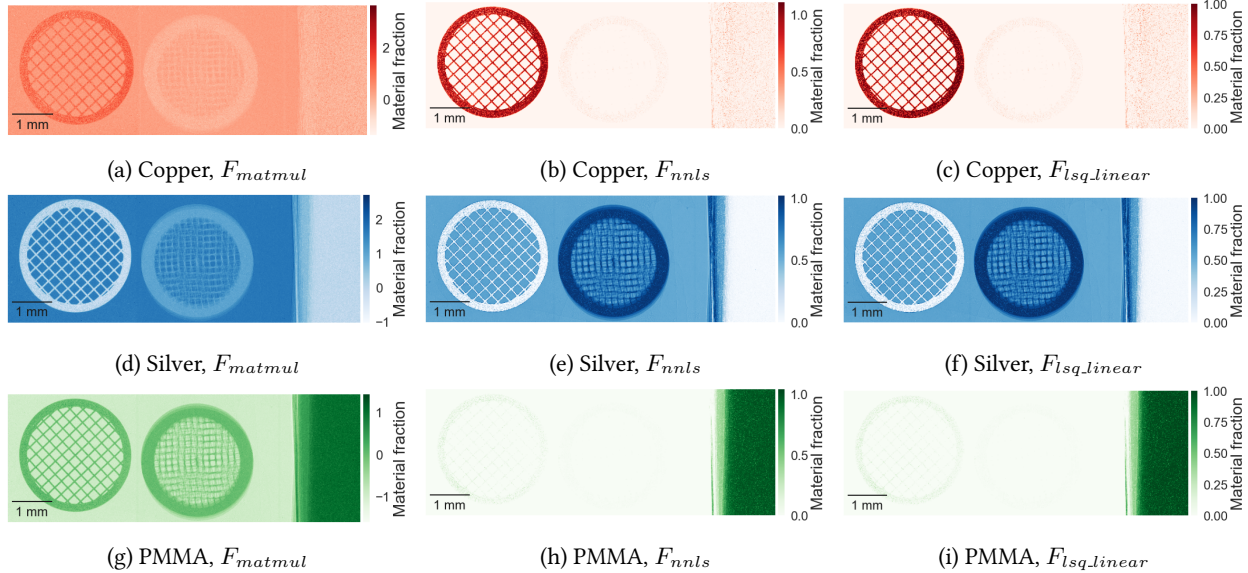


Figure 13: (a-c) Copper, (d-f) silver and (g-i) PMMA decomposed images of the copper and silver grid sample created with the three different decomposition methods F_{matmul} , F_{nnls} and $F_{lsq.linear}$.

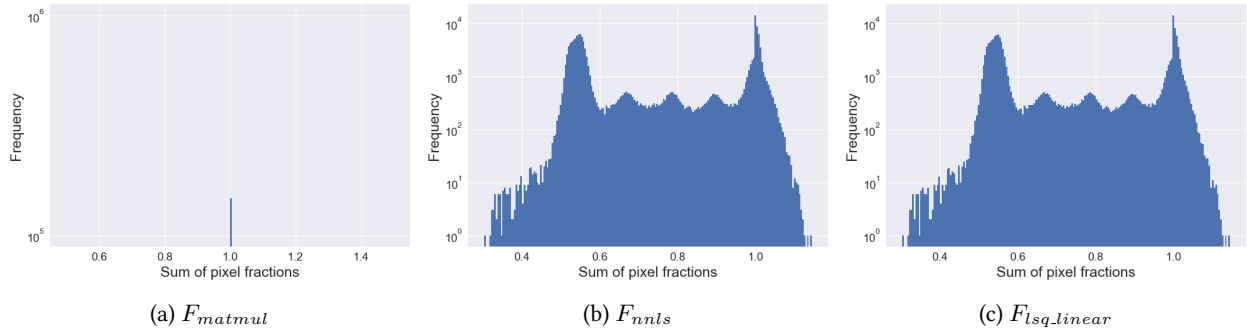


Figure 14: Histograms of the summations of the material fractions in each pixel for the copper and silver grid sample decomposed with the three material decomposition methods F_{matmul} (a), F_{nnls} (b) and F_{lsq_linear} (c).

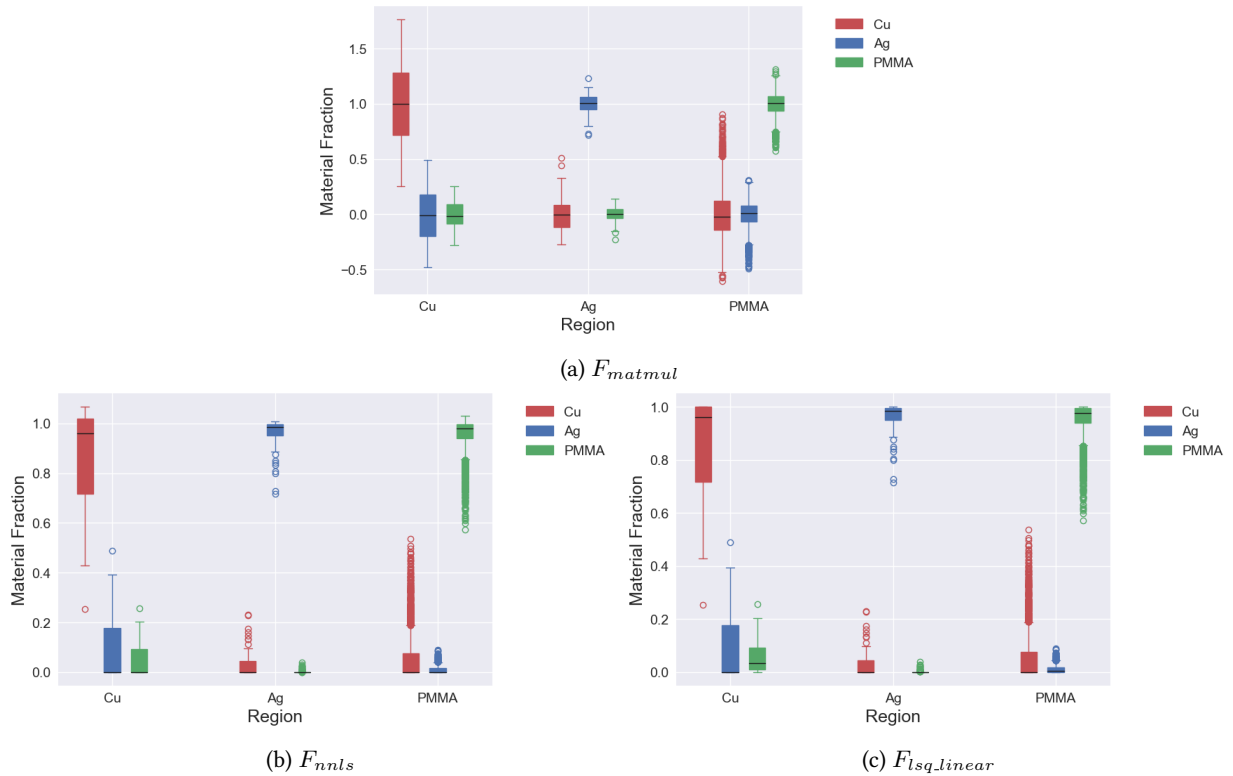


Figure 15: Box plots of the material fractions for the copper and silver grid sample decomposed into copper (red), silver (blue) and PMMA (green) images with the three material decomposition methods, F_{matmul} (a), F_{nnls} (b) and F_{lsq_linear} (c). The three regions are placed in each material and in the same place for all material images.

4.1 Copper and silver grids sample

The measured attenuation values in the copper, silver and PMMA regions of the sample for the different energy windows are presented in Figure 16. Compared to the silver and PMMA where no absorption edges are visible in the energy range, the presence of copper K-edge at 8.98 keV results in the drop in attenuation up to the 8 - 9.5 keV window and the increase in attenuation after it. Whereas the attenuation for silver and PMMA decreases from the same energy window toward higher energies. Based on this and on having none overlapping energy windows on

each side of the K-edge, the energy windows chosen to base the material decomposition on were 7.5 - 9 keV and 9 - 10.5 keV.

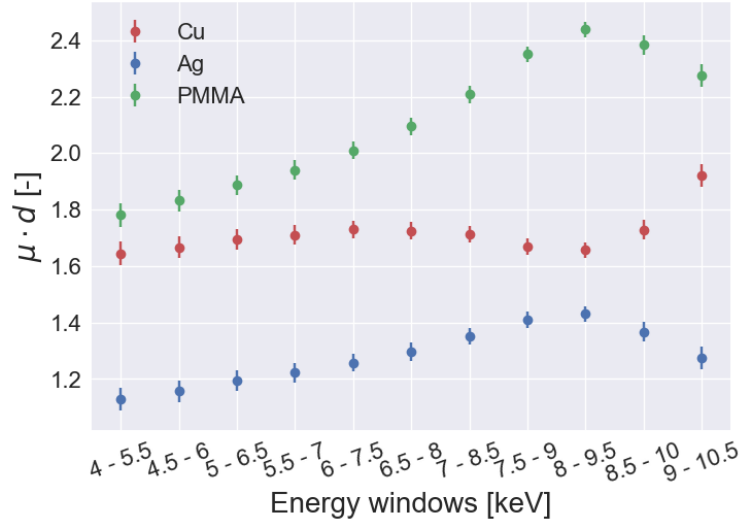
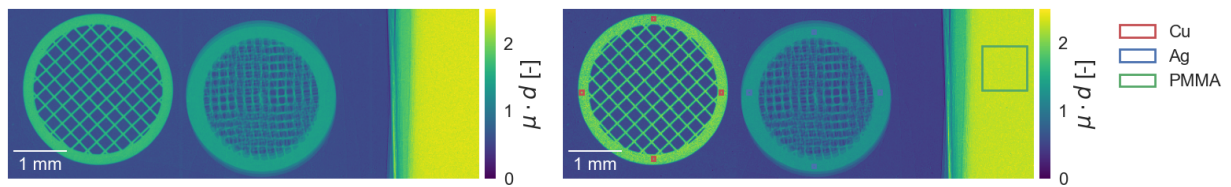


Figure 16: The measured attenuation $\mu \cdot d$ in 1.5 keV energy windows of the copper and silver grid sample radiographies. The regions used to calculate the values for each material are shown in Figure 17b.

The attenuation images of the chosen energy windows are shown in Figure 17. Based on these two images, the material decomposed images in Figure 18 were constructed. The two grids and the PMMA piece are well defined in each material image. There are some pixels with a low fractions of copper outside the grid and the same applies for the PMMA piece.

The grids and the PMMA piece were taped to a plastic card and due to the decomposition being made with only three materials, this background had to be assigned a fraction of some material. Hence, the silver decomposed image has a low fraction of silver in the background around the grids. The left edge of the PMMA piece is also assigned a higher fraction of silver and a lower fraction of PMMA.



(a) Lower energy window, 7.5 - 9 keV.

(b) Upper energy window, 9 - 10.5 keV.

Figure 17: The two images acquired for the (a) lower and (b) upper energy window images of the copper and silver grids sample used for the material decomposition. In the upper energy window image, the ROIs used for calculation of material decomposition attenuation values for the three materials are shown. The mean value of the four regions in the copper and silver grids were used.

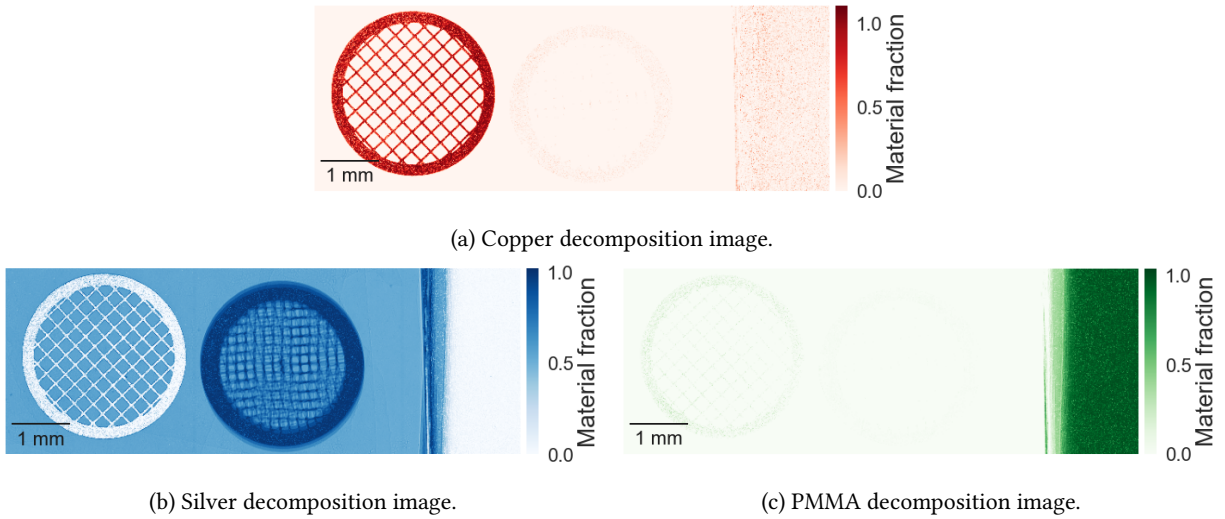


Figure 18: The material decomposition images of (a) copper, (b) silver and (c) PMMA of the copper and silver grid sample.

4.2 Copper cable and aluminium foil sample

In Figure 19a the regions used to calculate the attenuation plot in Figure 19b are shown. Similar to the copper grid, a increase in the attenuation is seen with increasing energy as expected. The aluminium regions do not decrease in attenuation but where the copper increases after the K-edge at 9 keV, the aluminium values stay relatively the same. Therefore, energy widows between 7.5 - 9 keV and 9 - 10.5 keV were used for the decomposition.

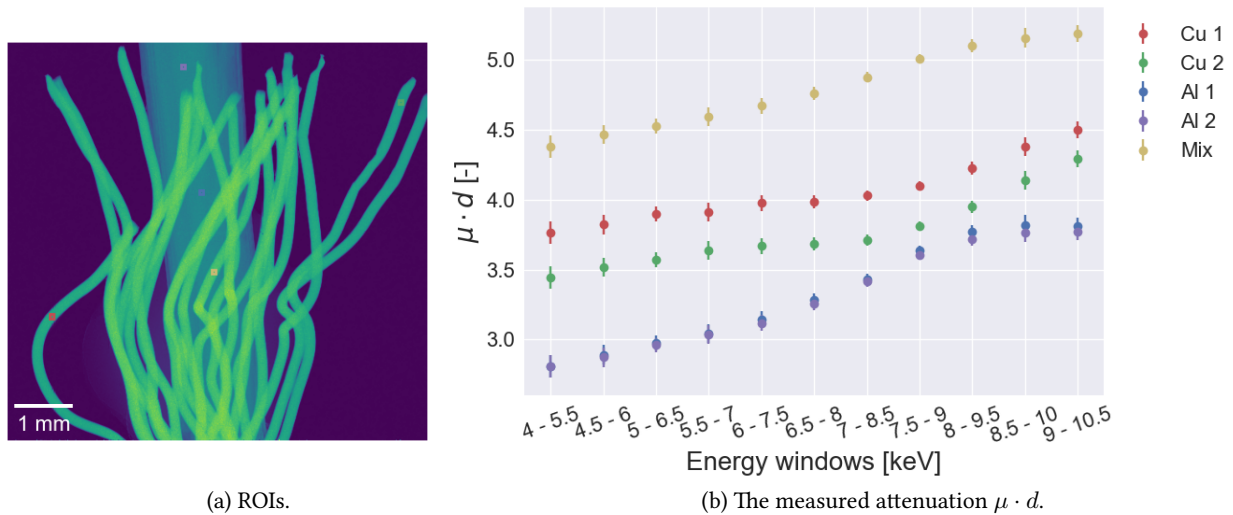


Figure 19: (a) The ROIs used for measurements of the attenuation $\mu \cdot d$ in the copper cable and aluminium foil sample radiographies. (b) Plot of the measured attenuation $\mu \cdot d$ in the ROIs in 1.5 keV energy windows.

Many streak artifacts due to beam hardening were affecting the two energy window images as seen in Figure 20. Because of that, a slice at the top of the sample was selected for decomposition as only three copper wires reached that far up. In the same figure, the regions chosen for decomposition attenuation values are shown. The CT reconstruction was done without any ring filtering which is very visible in the decomposed images in Figure 21. Reconstructions

were done both with and without ring filtering, but whereas the reconstructed slices became better with ring filtering, the decomposition inside the aluminium foil became worse as larger regions were distorted instead of the multiple thin rings seen in Figure 21.

In general, the decomposition into copper, aluminium and air was successful given the artifacts, with the copper cable clearly being decomposed and only a low incorrect copper fraction in the aluminium foil. As the aluminium foil was folded and squeezed together it is reasonable that some regions have a lower aluminium fraction.

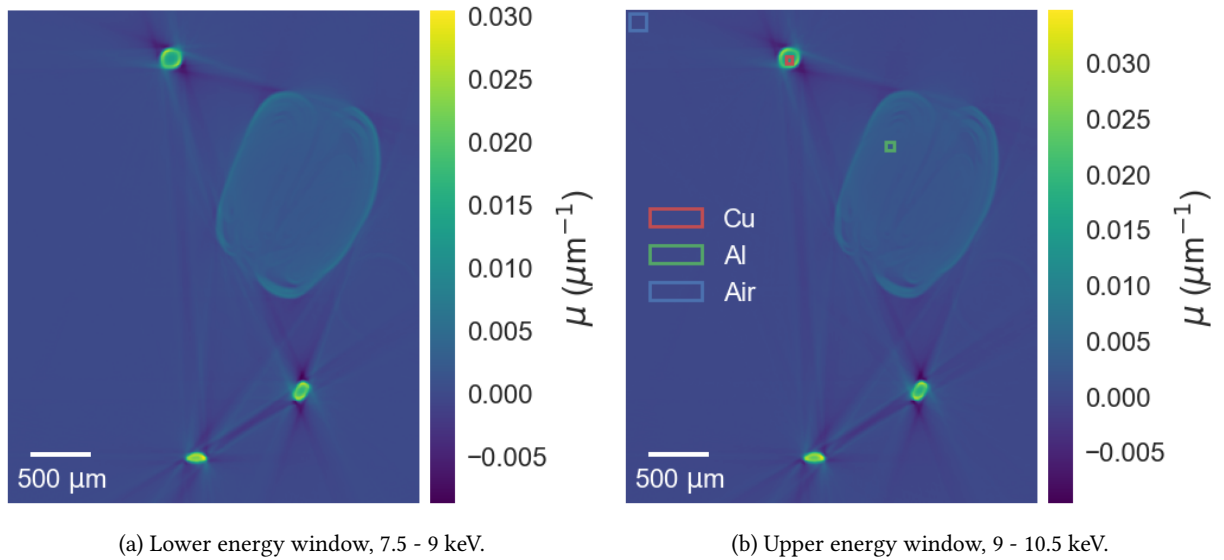
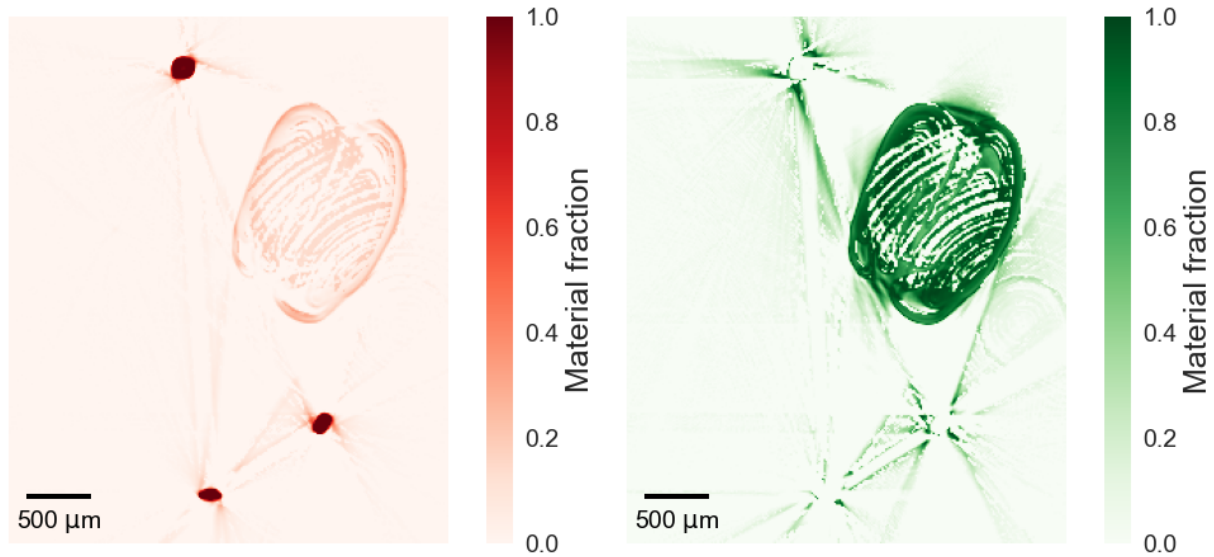
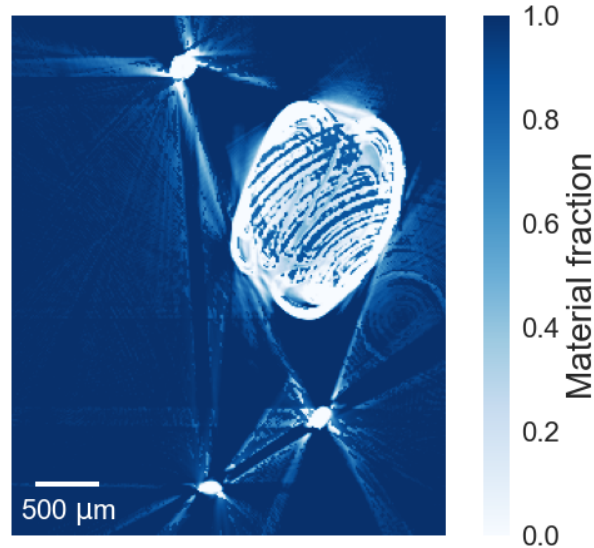


Figure 20: The reconstructed slices of the (a) lower and (b) upper energy windows of the copper cable and aluminium foil sample used for the material decomposition. In the upper energy window image, the ROIs used for calculation of material decomposition attenuation values for the three materials are shown.



(a) Copper decomposition image.

(b) Aluminium decomposition image.



(c) Air decomposition image.

Figure 21: The material decomposition images of (a) copper, (b) aluminium and (c) air of the CT reconstructed copper cable and aluminium foil sample slice.

4.3 MultiHance samples

In Figure 22, the ROIs and attenuation plot for the MultiHance radiographies are presented. Here, no clear effect of the gadolinium L-edges on the attenuation is visible as both water and the MultiHance concentrations plots seems to have the same shape, just with higher attenuation for higher concentrations. Because of this the energy spectrum calculations presented in Section 4.3.3 were done. Depositions were done with energy windows between 5 - 6.5 keV and 8 - 9.5 keV for the radiography and between 4 - 6 keV and 8 - 9.5 keV for the CT.

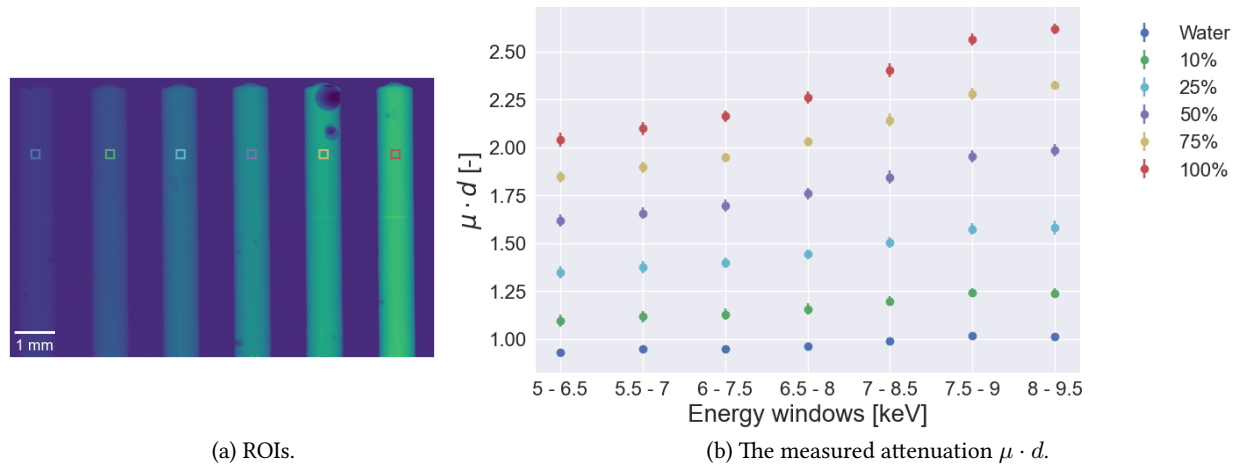


Figure 22: (a) The ROIs used for measurements of the attenuation $\mu \cdot d$ in the MultiHance sample radiographies. (b) Plot of the measured attenuation $\mu \cdot d$ in the ROIs in 1.5 keV energy windows.

4.3.1 Radiography

The energy window images and regions for decomposition values are shown in Figure 23 and the decomposition images of MultiHance, water and PMMA are shown in Figure 24. The decomposition of MultiHance is successful but the water and PMMA are hard to separate as there is not much difference between the materials. Since the MultiHance decomposition attenuation value were corrected before the decomposition, the MultiHance fraction is just below 0.6 and not 1 in the 100 % tube to the right which also contains some fractions of water and PMMA.

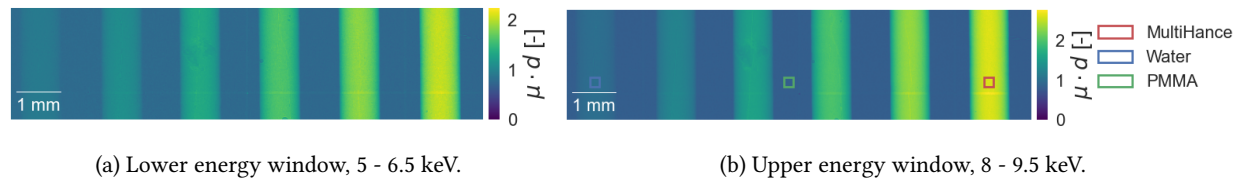


Figure 23: The two images acquired for the (a) lower and (b) upper energy windows of the gadolinium contrast agent sample used for the material decomposition. In the upper energy window image, the ROIs used for calculation of material decomposition attenuation values for the three materials are shown.

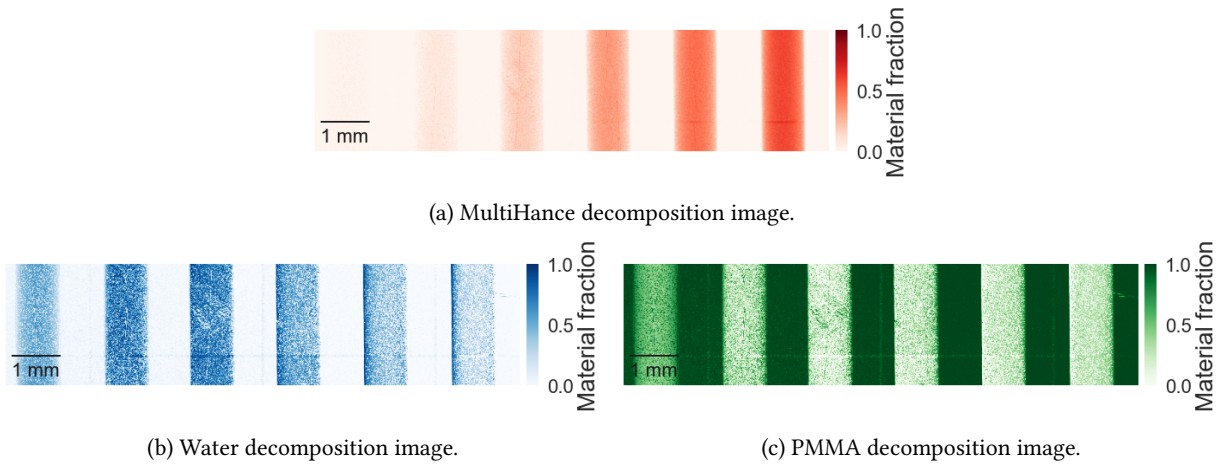


Figure 24: The material decomposition images of (a) MultiHance, (b) water and (c) PMMA calculated from the radiographies of the MultiHance contrast agent sample.

The calculated fractions in the center of the tubes are presented in the box plot in Figure 25a. Here the trouble of separating water and PMMA is very clear. To compare the MultiHance fractions to the expected concentrations in the tubes, the fractions were corrected so that all MultiHance were in the center 1 mm of the tube and not in the full thickness of the holder. This result is presented in Figure 25b where the measured MultiHance concentrations are in general slightly higher but in good agreement with the expected concentrations.

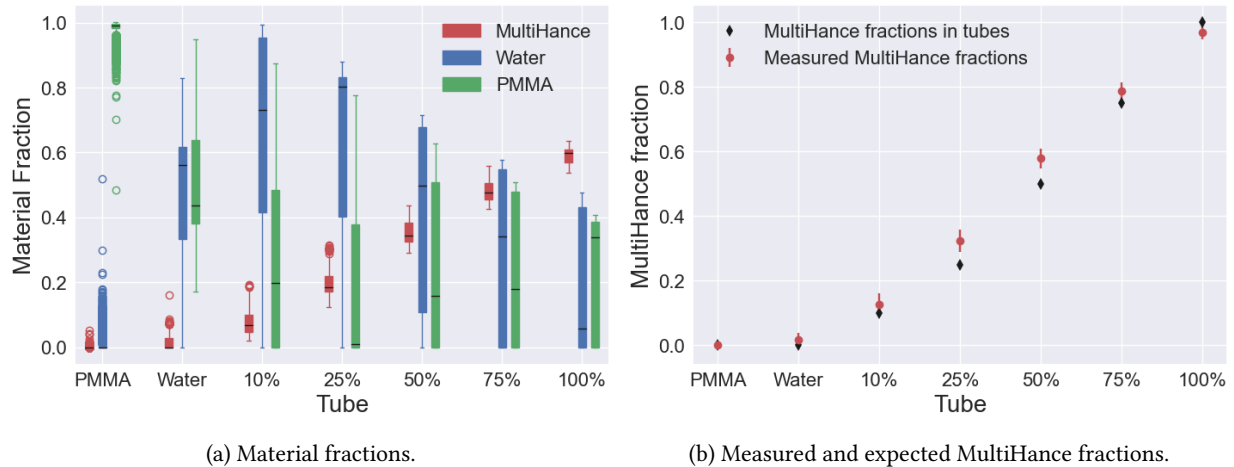


Figure 25: (a) Box plot of the material fractions in the center of the sample tubes for MultiHance and water fractions and regions between the tubes for the PMMA fractions. The MultiHance fractions presented here are the actual measured fractions, hence not compensated for the PMMA in the tube walls. (b) Comparison between the measured MultiHance fractions, here compensated for the PMMA in the tube walls, and the expected concentrations.

4.3.2 Computed tomography

In Figure 26 the selected slices from the CT reconstruction of the MultiHance sample are shown with the regions used for decomposition attenuation values. Like the radiography, the decomposition of MultiHance in Figure 27 is successful even though it is affected by beam hardening and ring artifacts. Also, the separation between water and PMMA is difficult for the CT decomposition as well. The decomposition was done with the three basis materials

being MultiHance, water and PMMA. Hence, the surrounding air must be allocated a material fraction of one of these materials. Therefore, the surrounding air is shown as PMMA since PMMA made the best fit for the calculations of the material fractions.

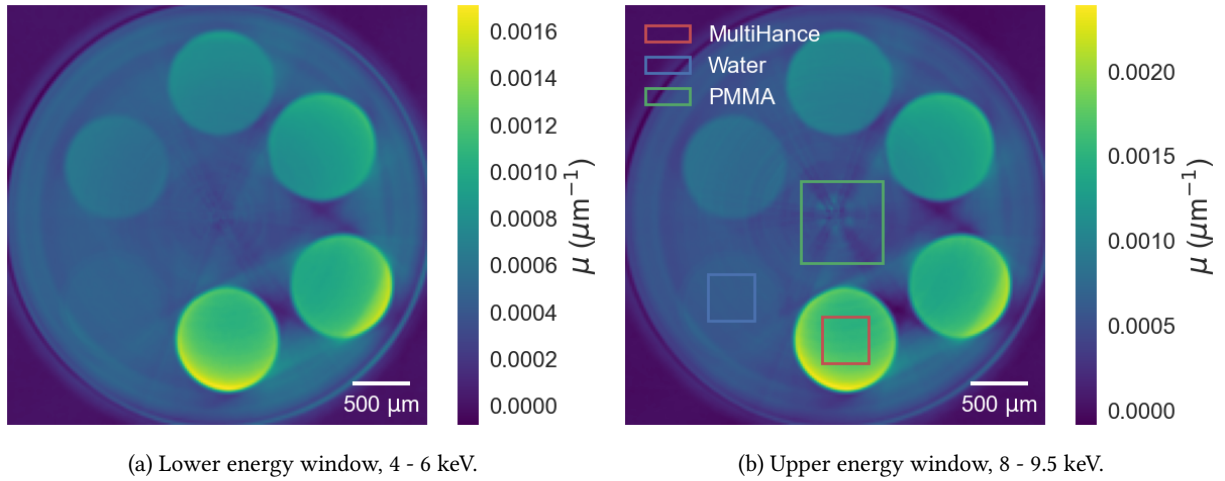
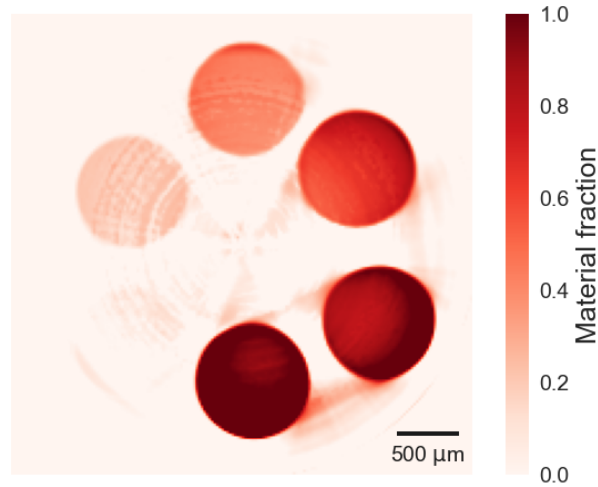
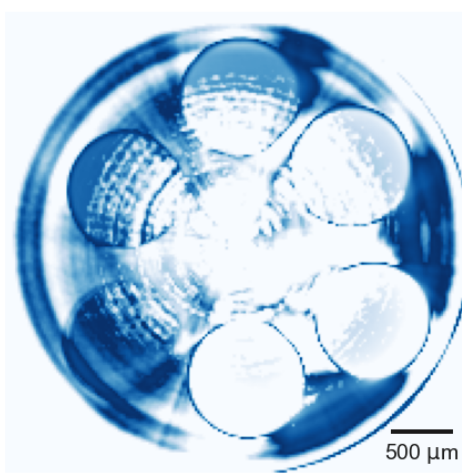


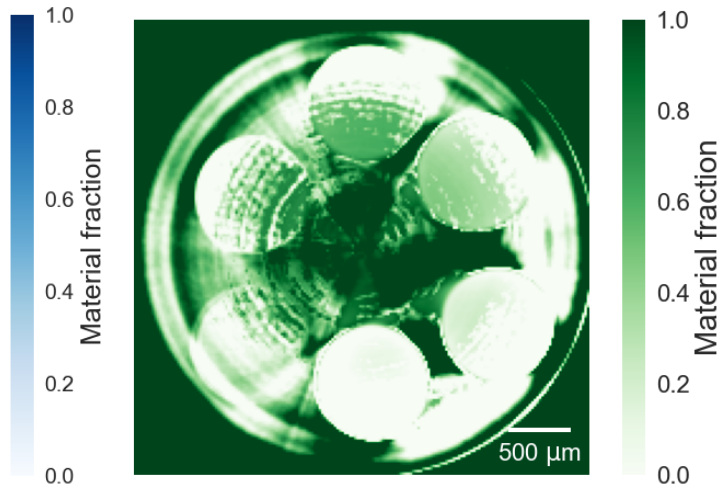
Figure 26: The reconstructed slices of the (a) lower and (b) upper energy windows of the MultiHance contrast agent sample used for the material decomposition. In the upper energy window image, the ROIs used for calculation of material decomposition attenuation values for the three materials are shown.



(a) MultiHance decomposition image.



(b) Water decomposition image.



(c) PMMA decomposition image.

Figure 27: The material decomposition images of (a) MultiHance, (b) water and (c) PMMA of the CT reconstructed MultiHance contrast agent sample slice. The effects of beam hardening and ring artefacts on the decomposition are here very clear.

In the box plot in Figure 28a the fractions in the center of the tubes and in the PMMA between the tubes are plotted. Like the radiography, the MultiHance fractions show more consistency than the water and PMMA fractions. The measured MultiHance fractions from the CT decomposition are compared to the expected concentrations in Figure 28b and these are fairly similar but in general slightly higher for the measured fractions.

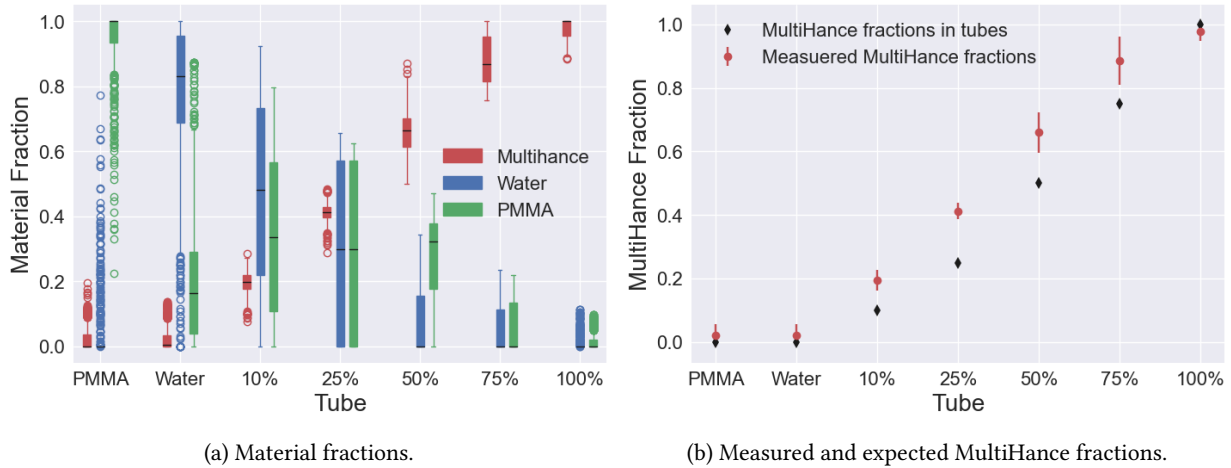


Figure 28: (a) Box plot of the material fractions from the CT decomposition measured in the center of the tubes for MultiHance and water fractions and in the center of the whole sample for the PMMA fraction in similarity with the decomposition attenuation values ROIs. (b) Comparison between the measured MultiHance fractions from the CT decomposition and the expected concentrations.

4.3.3 Energy spectrum

The simulated spectra of the detected photons and transmission are presented in Figures 29a and 29b. The values on the Y-axes are plotted as arbitrary units, a.u.. Shown in red and green are just MultiHance and MultiHance and the PMMA in the holder’s wall respectively. The effect of the gadolinium L-edges is most clear in the transmission plot, Figure 29b, but the actual difference before and after the edge is negligible, especially when it is averaged out over a 1.5 keV window before and after the edge. Therefore it is reasonable that no differences in attenuation were shown in the attenuation plot in Figure 22b.

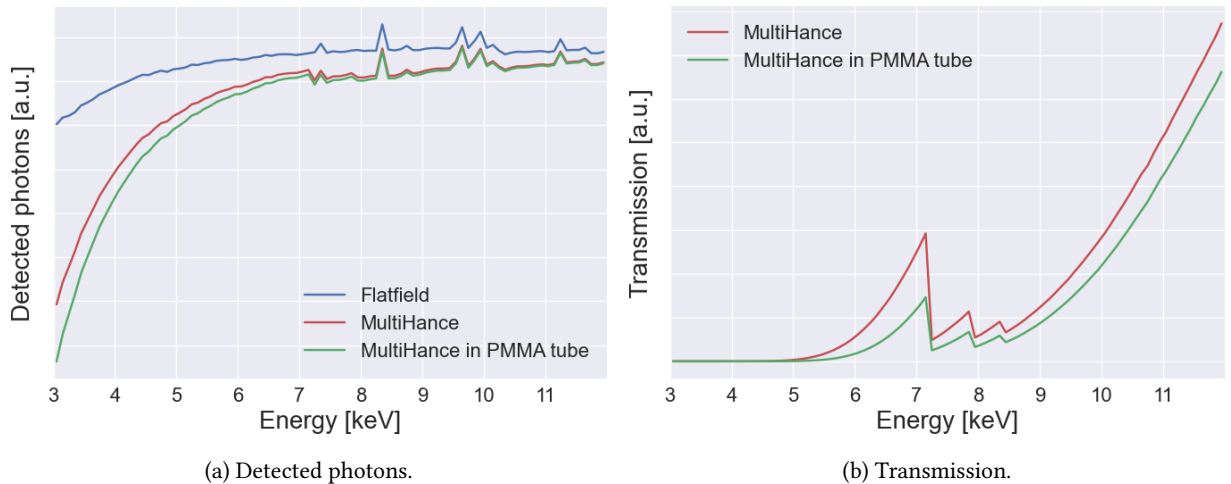


Figure 29: (a) Simulated graph of detected photons as a function of photon energy. Y-axis is in logarithmic scale. (b) Simulated graph of transmission as a function of photon energy where the effect of the L-edges of gadolinium are seen between 7 keV and 9 keV. Y-axis is in linear scale.

4.4 Atherosclerotic plaque sample

For the plaque sample radiographies, ROIs were selected both in the calcification, the paraffin or soft tissue and the background as seen in Figure 30a. The attenuation in these regions are plotted in 1.5 keV energy windows in Figure 30b. Regions 1 and 2 were placed in the large calcification and show a slight increase in the slope of the plots after the iron K-edge at 7.11 keV. Region 3 has a more steady increase through all energy windows and regions 4 and 5 and the background show almost the same attenuation in all energy windows. For the decomposition, a lower energy window between 4 - 7 keV and an upper energy window between 7.5 - 9 keV were selected and the reconstructed slices chosen for decomposition are seen in Figure 31.

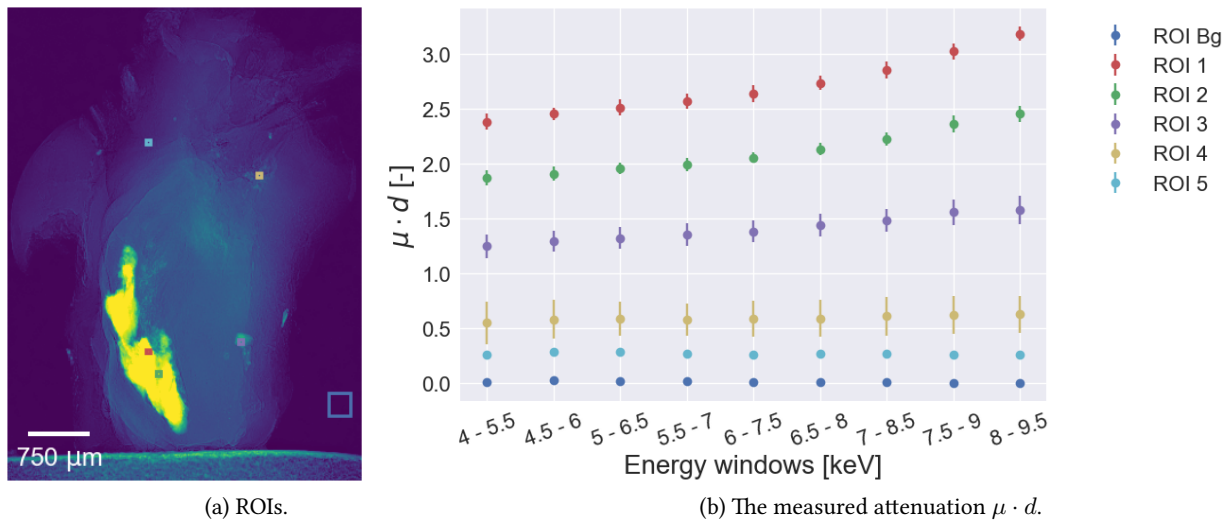


Figure 30: (a) The ROIs used for measurements of the attenuation $\mu \cdot d$ in the plaque sample radiographies. (b) Plot of the measured attenuation $\mu \cdot d$ in the ROIs in 1.5 keV energy windows. ROI Bg is a ROI set in the background.

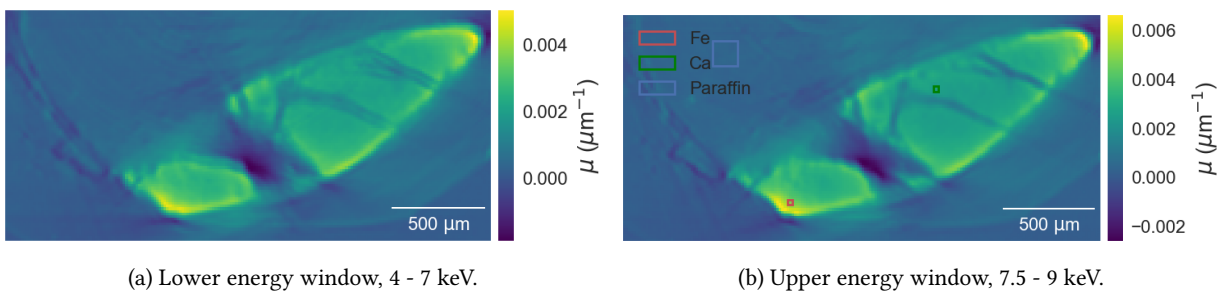


Figure 31: The reconstructed slices of the (a) lower and (b) upper energy windows of the plaque sample used for the material decomposition are presented. In the upper energy window image, the ROIs used for calculation of material decomposition attenuation values for the three materials are shown.

The region for the paraffin decomposition attenuation value was placed outside the larger calcification that seemed to be free from any calcifications and artifacts. The region defining iron was placed in an area where the attenuation increased to the higher energy window image. For calcium the attenuation should in theory decrease with higher energy but as seen in Figure 30b, regions with just paraffin or small calcifications resulted in a constant or slowly increasing attenuation. Therefore, a region inside the calcification where the attenuation only had a small increase were chosen.

In Figure 32, the material decomposed images are presented. The iron and calcium images show a reasonable distribution of the materials within the calcification.

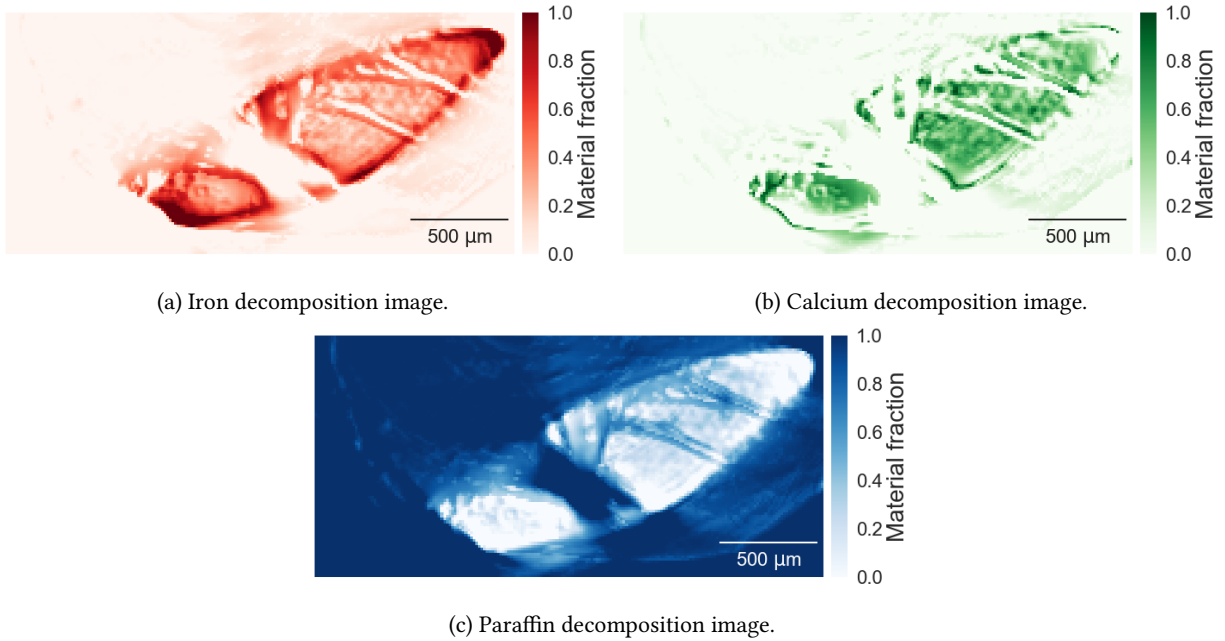


Figure 32: The material decomposition images of (a) iron, (b) calcium and (c) paraffin of the CT reconstructed plaque sample slice.

4.4.1 Verification of multiple materials in calcification

As the exact content and distribution of materials in the plaque sample were known, a simple simulation of how the sample would look like if only one material was present was done. Based on the lower energy radiography image in Figure 33a and the tabulated value of the attenuation coefficient [7] of calcium in the lower energy, 556 cm^{-1} , a simulated thickness of the sample was calculated. The thickness image is shown in Figure 33b and corresponds to the sample consisting of only calcium. The theoretical attenuation coefficient of calcium decreases to 160 cm^{-1} for the upper energy window. With this value and the simulated thickness multiplied, an upper energy window image was created, Figure 33c, whose image values then represents the values if the sample would consist of only calcium in the upper energy window. A difference image between this image and the acquired upper energy window, Figure 33d, is shown in Figure 33e where the acquired image values are subtracted from the created ones.

Focusing on the calcifications in the sample, the acquired image values in the upper energy are higher than the simulated ones resulting in the negative values in the difference image. This could be explained by the presence of iron in the calcification as the iron K-edge creates a higher attenuation in the upper energy window.

The method was also tested on the radiographies of the copper cable and aluminium foil sample and the result is presented in Figure 34.

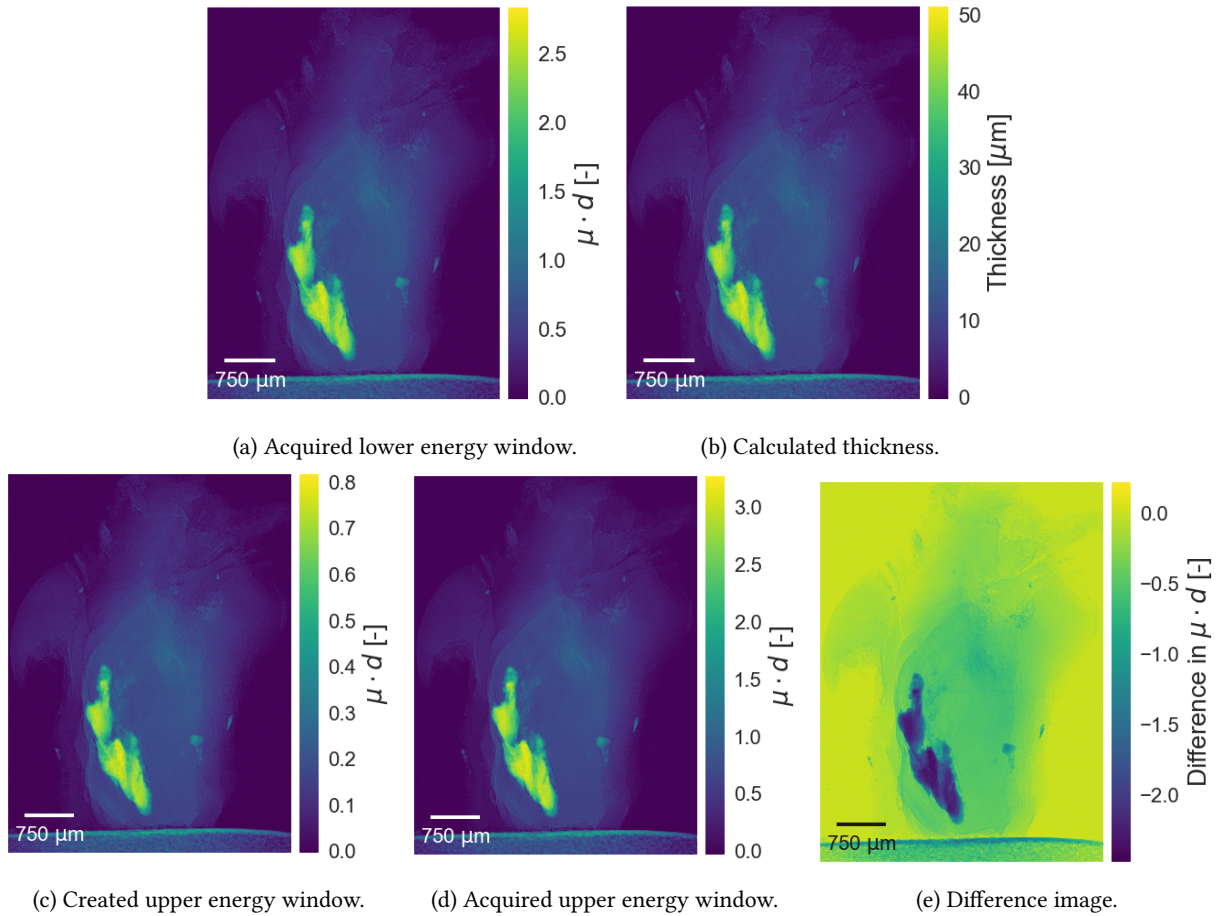


Figure 33: Thickness simulation of the plaque sample with (a) the lower energy window image used to create (b) the calculated thickness of solid calcium. (c) The created upper energy window image that is compared to (d) the acquired upper energy window image. (e) The difference between calculated an acquired upper energy window. The plaque is mounted to double sided tape which is seen at the bottom of the images.

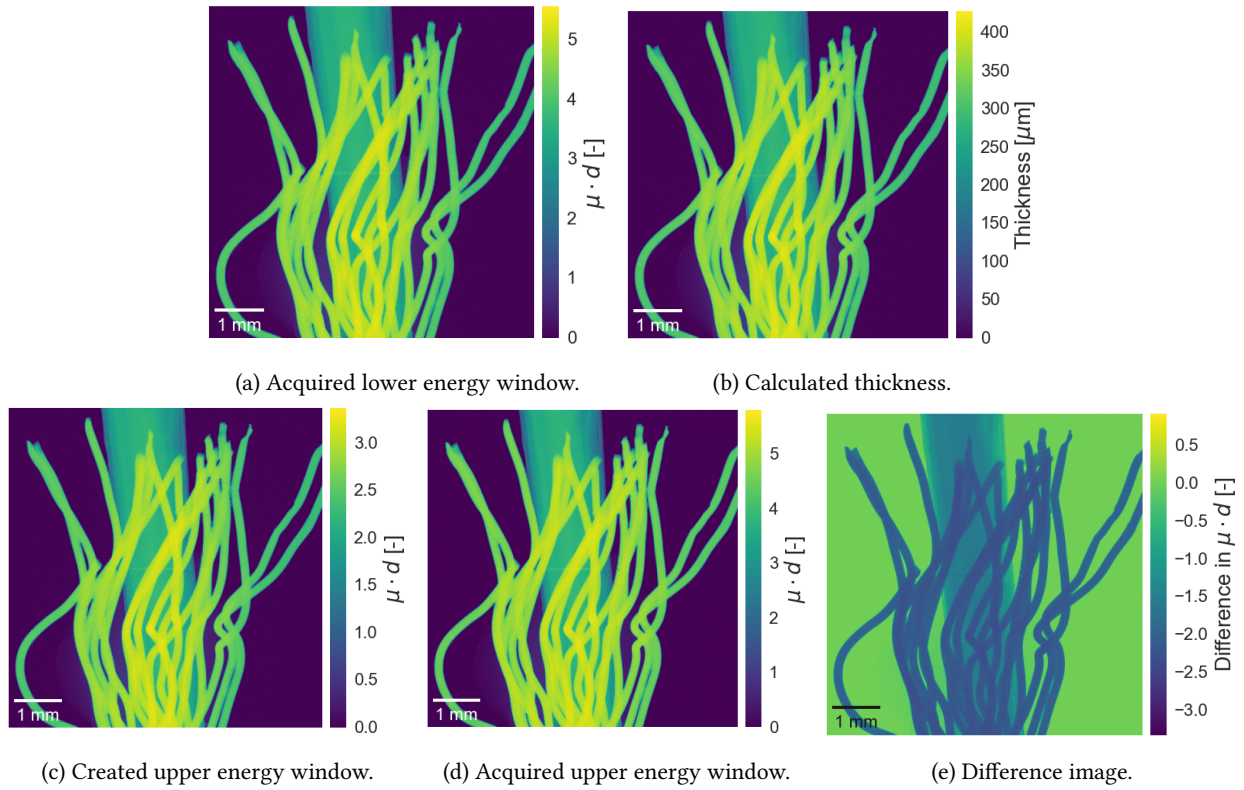


Figure 34: Thickness simulation of copper cable and aluminium foil sample with (a) the lower energy window image used to create (b) the calculated thickness of solid aluminium. (c) The created upper energy window image that is compared to (d) the acquired upper energy window image. (e) The difference between calculated an acquired upper energy window.

5 Discussion

Judging by the verification samples, the implemented decomposition method resulted in reasonable decomposed material images. Since the impact of the gadolinium L-edges on the MultiHance samples was not measurable it showed that the decomposition method also worked for samples without an absorption edge as long as there was a difference in attenuation between the materials. It also worked for the quantification of the material concentrations.

The width of the energy windows were set to be at least 1.5 keV to ensure a sufficient amount of counts in the images but without averaging the attenuation value over a too large energy range, and thus reducing the difference between energy windows, as well as not having a energy window smaller than the detectors energy resolution. For the CT acquisitions of the MultiHance and plaque samples, slightly larger windows were set for the lower energy windows as this was estimated to only have a small impact on the attenuation value but the increase in counts was to be beneficial for the reconstruction.

Some a priori knowledge of the sample's content is necessary to choose the regions for the decomposition attenuation values for the materials. Depending on how these values are picked by the operator the resulting decomposition could be very different. It is also during this selection of values, the definition of which material is which in the sample is defined. Hence, what is decomposed as a specific material is decided by the operator and therefore knowledge of the sample and what to expect regarding attenuation coefficients is necessary.

The material fractions do also not represent the fraction of the actual material but the fraction of what is stated by the operator to be 100 % of the material. Taking the plaque sample as an example, an iron material fraction of 1 does not mean that there is only solid iron in that volume but that it is the same amount of iron as that amount stated to be only iron by the operator.

To make the method less operator dependent, the decomposition attenuation value matrix for CT decompositions could be constructed in a calibration stage. By creating a sample similar to the cylindrical MultiHance PMMA holder and filling the tubes with solutions or solids of the desired materials, the values for the matrix could be selected. Defining what is 100 % of a material from a calibration sample would also make it possible to compare the distribution and concentration of materials in different samples. For the implemented method this is not possible as the definitions are based on the individual sample.

The calculation of the material fractions were done with three different methods as described in Section 3.3. The matrix multiplication, F_{matmul} , correctly solves Equation 7 but does not take any of the a priori knowledge into account resulting in non-valid material fractions even though the mean value of different regions are correct. For the two functions that put constraints on the material fractions, F_{npls} and $F_{lsq.linear}$, the values of the total fraction in each voxel are instead spread around 1 as a result of solving of the least squares problems. For the radiographies, this is more of a benefit than a problem as the sample thickness may vary between pixels and one pixel may contain less material than another. For CT decomposition, this is not an issue since every voxel has the same volume.

The difference between F_{npls} and $F_{lsq.linear}$, where F_{npls} only has a non-negative constraint is very small, especially if the material decomposition values are correctly defined based on regions with the highest concentration of the given material in the images. If this is done, the highest possible material fraction would be 1. Hence yielding the same result with the two methods. One large benefit with the non-negative F_{npls} is that the computational time is considerably shorter. Altogether, it was decided that the non-negative constrained method was the better choice for the material decomposition.

With the addition of more energy windows, more materials in a sample would in theory be able to be decomposed, but would need to be tested. This could be used if a sample contained more distinct materials, for instance another material with a visible absorption edge, or to separate a fourth material such as the surrounding air. The removal of surrounding air could also possibly be done by excluding pixels with attenuation values equal to or close to zero.

5.1 MultiHance contrast agent sample

The actual diluted MultiHance concentrations are probably not the exact concentrations as stated. The dilution was done by pipetting desired volumes of MultiHance and water into a plastic vial. Here, there might be some small differences between the desired volumes and those that were actually mixed. When filled in the tubes in the PMMA holder, the water in the concentrations evaporated but the gadolinium remained in the remaining solution resulting in an increase of the gadolinium concentration. Multiple attempts of sealing the tubes to minimize the evaporation were done with different combinations of tape, paraffin wax, nail polish and epoxy glue. In the end, it was decided that the epoxy glue was the best choice. But even then, some evaporation and leakage could not be avoided. During the CT acquisition that took around 60 hours, the solution surface in the tubes could be seen to decrease between the projections. Hence, the MultiHance concentrations increased even during the measurements.

Before filling the tubes in the PMMA holders, the concentrations were mixed and stored in sealed plastic vials. For the CT acquisition presented in the thesis, the concentrations were mixed just before the start of the measurement. But for the radiographies presented here, the concentrations were diluted a few days before filling the tubes for the measurement. Even though they were stored in a closed vial some vaporization of the water could occur resulting in a slightly higher concentration. Because of this, the expected concentrations of MultiHance may not be exact which should be kept in mind when compared to the measured fractions.

The decomposition of the radiography sample was done with some corrections of the decomposition attenuation values so the MultiHance fraction would represent MultiHance and not the combination of MultiHance and PMMA which would be the case if the average image value were chosen. With this correction the fraction of PMMA is also not 0 in the 100 % tube. Hence, the results correspond to the real sample in a better way with the corrections made. To then compare the MultiHance fractions to the expected concentrations, the fractions were corrected based on the knowledge that MultiHance would only be inside the tube. For the CT decomposition no corrections of this sort were necessary as regions were selected inside the tubes for decomposition attenuation values and material fractions.

For both radiographies and CT, the decomposition of MultiHance works well and the material fractions are in reasonable agreement with the expected concentrations. Water and PMMA have similar attenuation characteristics making it difficult to separate them. In the material decomposed images of the radiographies in Figure 24 it is visible that the separation between water and PMMA in regions only containing PMMA is possible but where both materials coexist, the materials are mistaken for each other. This is also seen in the box plot in Figure 25a where the large fraction variations within the tubes are shown with the large boxes. The separation between water and PMMA is even harder for the CT reconstructed slices where ring artifacts and beam hardening leads to a severe variation in attenuation values in the energy window images.

During the measurements of the MultiHance samples, it was suspected that the effect of the gadolinium L-edges could be measured. The suspicion was based on the attenuation plots for the different materials having a similar shape and when compared to the copper and silver grid sample where the effect of the copper K-edge were apparent. Therefore, the simulated graphs of detected photons and transmission, seen in Figures 29a and 29b, were created, and made it clear that the difference in attenuation between the two energy windows was too small to be measured. The figures display both MultiHance on its own with a thickness of the tube diameter and filled in the PMMA holder. For the effect of the L-edges to be measurable, the overall attenuation would have had to be lower. Therefore a reduction in both the thickness of the tube and the holder would have been necessary. Attempts of using Kapton tubes as a holder were done but were not feasible due to problems regarding filling, sealing and mounting of the tubes.

5.2 Atherosclerotic plaque sample

The selection of regions representing each material in the plaque sample was tricky as no areas containing only iron or calcium were known. The selections of these regions would highly impact the decomposition. To select the regions a difference image between the energy window images was studied. The iron decomposition attenuation value was selected from an area with one of the highest increases of attenuation value. Regions with calcium would

be expected to decrease in attenuation value but the only regions where this happened were places that were clearly influenced by artifacts. Therefore, a region inside the calcification with only a small increase in attenuation was chosen. With these adjustments from what were expected for the calcium regions in regards of attenuation, the resulting decomposition into iron, calcium and paraffin shows a reasonable distribution of the materials. The distribution of iron and calcium is similar to those shown in hematological staining of simulated plaques where iron and calcium had been injected into plaques [31].

Since the actual composition of the plaque was unknown, the thickness simulation of the sample was done to verify that the calcification consisted of at least two materials. Hence, that the material decomposition of it into iron and calcium is justifiable. Calcium was chosen for the single material thickness calculation as it in theory would decrease the attenuation value and regions containing iron would stand out due to the increase in attenuation value after the K-edge. All pixels in the calcification had a higher measured than calculated value in the upper energy window, resulting in negative values in the difference image. This is the same problem as the one for the selection of the decomposition attenuation value of calcium. Since it is a calcification, there is known to be calcium in it. Therefore it is assumed that regions with a slight increase in attenuation value between the energy windows is calcium. This is consistent with that also the soft tissue and paraffin wax increases in attenuation value. But there are regions within the calcification with a larger difference between calculated and measured values. These regions could be explained by the presence of iron due to hemorrhage which would increase the attenuation because of the effect of the iron K-edge on the attenuation.

The same simulation was done for the copper cable and aluminium foil sample with aluminium as the base material. In similarity with the calcium, aluminium would show a lower attenuation in the higher energy window but a slightly higher value is measured. This further justifies the selection of calcium values as there is some process in the detection, resulting in the measured increase of attenuation where it in fact should decrease. The copper regions in the thickness simulation show a larger difference than the aluminium regions which is expected with regards to the copper K-edge. Regions where the copper cable overlaps, hence having a larger quantity of copper, show the largest difference. Based on this, it is reasonable that the regions with the largest difference in the plaque sample contains more iron.

6 Conclusions

The implemented material decomposition method for X-ray imaging in the low energy range presented in this thesis works for both constructed samples with a known content as well as biomedical samples. It performs a reasonable quantification of the material concentrations, in general measuring a slightly higher concentration than expected. The measured material fractions are sample specific and can not be compared between samples.

A priori knowledge of the samples is necessary for the decomposition to work properly since important steps, such as the selection of energy windows and decomposition attenuation values, in the method are performed manually by the operator and are of great importance for a successful material decomposition.

The low energy range puts limitations on the sample's thickness and material content. To separate materials of similar attenuation, an adsorption edge in one material had to be within the measurable energy range. The sample also had to be thin enough for this edge to have a measurable affect on the spectrum.

The CT decomposition is largely influenced by artifacts in the reconstructed slices but the decomposition is still possible. Ring filtering during the reconstruction improved the decomposition for some but not all samples.

Future work on this method could be to implement calibration samples for different materials. With known concentrations of the materials, decomposition attenuation values could be measured and used for the decomposition instead of obtaining the values from the individual samples. This would make the method less operator dependent as well as enabling comparison of material fractions between samples. More energy windows could also be added to the decomposition method, which theoretically would enable decomposition of more materials in a sample.

7 Acknowledgements

I would like to thank my supervisors, Till Dreier and Martin Bech, for their help, support and encouragement during the thesis and to express my gratitude to the whole X-ray group for making me feel welcomed into the group.

Thanks to Jan Hultqvist for the production of the PMMA holders and Isabel Goncalves for providing the plaque sample.

Finally, I would like to thank family and friends for their unconditional support.

8 References

- [1] R. E. Alvarez and A. Macovski, "Energy-selective reconstructions in X-ray computerised tomography," *Physics in Medicine and Biology*, vol. 21, no. 5, pp. 733–744, 1976.
- [2] C. J. Bateman, D. Knight, B. Brandwacht, J. M. Mahon, J. Healy, R. Panta, R. Aamir, K. Rajendran, M. Moghiseh, M. Ramyar, D. Rundle, J. Bennett, N. De Ruiter, D. Smithies, S. T. Bell, R. Doesburg, A. Chernoglazov, V. B. Mandalika, M. Walsh, M. Shamshad, M. Anjomrouz, A. Atharifard, L. V. Broeke, S. Bheesette, T. Kirkbride, N. G. Anderson, S. P. Gieseg, T. Woodfield, P. F. Renaud, A. P. Butler, and P. H. Butler, "MARS-MD: Rejection based image domain material decomposition," *Journal of Instrumentation*, vol. 13, no. 5, 2018.
- [3] P. V. Granton, S. I. Pollmann, N. L. Ford, M. Drangova, and D. W. Holdsworth, "Implementation of dual- and triple-energy cone-beam micro-CT for postreconstruction material decomposition," *Medical Physics*, vol. 35, no. 11, pp. 5030–5042, 2008.
- [4] M. Patino, A. Prochowski, M. D. Agrawal, F. J. Simeone, R. Gupta, P. F. Hahn, and D. V. Sahani, "Material separation using dual-energy CT: Current and emerging applications," *Radiographics*, vol. 36, no. 4, pp. 1087–1105, 2016.
- [5] M. J. Willeminck, M. Persson, A. Pourmorteza, N. J. Pelc, and D. Fleischmann, "Photon-counting CT: Technical principles and clinical prospects," *Radiology*, vol. 289, no. 2, pp. 293–312, 2018.
- [6] C. A. Carlsson and G. A. Carlsson, "Basic physics of X-ray imaging," *Linköping University*, pp. 3–29, 1996.
- [7] M. Berger, J. Hubbell, S. Seltzer, J. Chang, J. Coursey, R. Sukumar, D. Zucker, and K. Olsen, "XCOM: Photon Cross Section Database (version 1.5)," 2010.
- [8] G. F. Knoll, "Radiation Detection and Measurement. 4th ed. New York: Wiley," 2010.
- [9] S. Leng, M. Bruesewitz, S. Tao, K. Rajendran, A. F. Halaweish, N. G. Campeau, J. G. Fletcher, and C. H. McCollough, "Photon-counting detector CT: System design and clinical applications of an emerging technology," *Radiographics*, vol. 39, no. 3, pp. 729–743, 2019.
- [10] D. Krapohl, *Monte Carlo and Charge Transport Simulation of Pixel Detector Systems*. 2015.
- [11] DECTRIS, "DIRECT Detection [Internet]. 2019 [cited January 2021]. Available from: <https://www.dectris.com/technology/hybrid-photon-counting/direct-detection/>."
- [12] I. Johnson, A. Bergamaschi, H. Billich, S. Cartier, R. Dinapoli, D. Greiffenberg, M. Guizar-Sicairos, B. Henrich, J. Jungmann, D. Mezza, A. Mozzanica, B. Schmitt, X. Shi, and G. Tinti, "Eiger: A single-photon counting x-ray detector," *Journal of Instrumentation*, vol. 9, no. 5, 2014.
- [13] J. Jakubek, "Precise energy calibration of pixel detector working in time-over-threshold mode," *Nuclear Instruments and Methods in Physics Research, Section A: Accelerators, Spectrometers, Detectors and Associated Equipment*, vol. 633, no. SUPPL. 1, pp. S262–S266, 2011.
- [14] P. Križan, "Photon detectors," *Handbook of Particle Detection and Imaging*, pp. 298–311, 2012.
- [15] DECTRIS, "Silicon Sensors [Internet]. 2019 [cited January 2021]. Available from: <https://www.dectris.com/technology/sensors/silicon-sensors/>."
- [16] R. A. Ketcham and R. D. Hanna, "Beam hardening correction for X-ray computed tomography of heterogeneous natural materials," *Computers and Geosciences*, vol. 67, pp. 49–61, 2014.
- [17] J. Sijbers and A. Postnov, "Reduction of ring artefacts in high resolution micro-CT reconstructions," *Physics in Medicine and Biology*, vol. 49, no. 14, 2004.

- [18] X. Wang, D. Meier, K. Taguchi, D. J. Wagenaar, B. E. Patt, and E. C. Frey, “Material separation in x-ray CT with energy resolved photon-counting detectors,” *Medical Physics*, vol. 38, no. 3, pp. 1534–1546, 2011.
- [19] C. T. Badea, X. Guo, D. Clark, S. M. Johnston, C. D. Marshall, and C. A. Piantadosi, “Dual-energy micro-CT of the rodent lung,” *American Journal of Physiology-Lung Cellular and Molecular Physiology*, vol. 302, pp. L1088–L1097, 5 2012.
- [20] S. Handschuh, C. J. Beisser, B. Ruthensteiner, and B. D. Metscher, “Microscopic dual-energy CT (microDECT): a flexible tool for multichannel ex vivo 3D imaging of biological specimens,” *Journal of Microscopy*, vol. 267, no. 1, pp. 3–26, 2017.
- [21] S. Lee, Y. N. Choi, and H. J. Kim, “Quantitative material decomposition using spectral computed tomography with an energy-resolved photon-counting detector,” *Physics in Medicine and Biology*, vol. 59, no. 18, pp. 5457–5482, 2014.
- [22] S. Ehn, T. Sellerer, K. Mechlem, A. Fehringer, M. Epple, J. Herzen, F. Pfeiffer, and P. B. Noël, “Basis material decomposition in spectral CT using a semi-empirical, polychromatic adaption of the Beer–Lambert model,” *Physics in Medicine and Biology*, vol. 62, pp. N1–N17, 1 2017.
- [23] S. Beck, T. Sellerer, K. Mechlem, J. Bodden, F. Meurer, A. Sauter, J. Herzen, F. Pfeiffer, and D. Pfeiffer, “Photon-counting spectral basis component material decomposition for musculoskeletal radiographs,” *Scientific Reports*, vol. 10, p. 13889, 12 2020.
- [24] E. Roessl and R. Proksa, “K-edge imaging in x-ray computed tomography using multi-bin photon counting detectors,” *Physics in Medicine and Biology*, vol. 52, no. 15, pp. 4679–4696, 2007.
- [25] “Technical Specifications EIGER2 R 500K Detector Systems,” tech. rep., 2018.
- [26] B. Warning, “MultiHance Injection,” vol. 505, no. 4, pp. 1–22, 2004.
- [27] “User Manual EIGER2 R 500K Detector Systems,” tech. rep., 2018.
- [28] W. van Aarle, W. J. Palenstijn, J. Cant, E. Janssens, F. Bleichrodt, A. Dabrovolski, J. De Beenhouwer, K. Joost Batenburg, and J. Sijbers, “Fast and flexible X-ray tomography using the ASTRA toolbox,” *Optics Express*, vol. 24, no. 22, p. 25129, 2016.
- [29] W. van Aarle, W. Jan Palenstijn, J. De Beenhouwer, T. Altantzis, S. Bals, K. Joost Batenburg, and J. Sijbers, “The ASTRA Toolbox: A platform for advanced algorithm development in electron tomography,” *Ultramicroscopy*, vol. Volume 157, pp. 35–47, 2015.
- [30] L. M. Lohse, A.-I. Robisch, M. To, S. Maretzke, M. Krenkel, J. Hagemann, and T. Salditt, “A phase-retrieval toolbox for X-ray holography and tomography,” pp. 852–859, 2020.
- [31] J. Wang, N. Garg, X. Duan, Y. Liu, S. Leng, L. Yu, E. L. Ritman, B. Kantor, and C. H. McCollough, “Quantification of iron in the presence of calcium with dual-energy computed tomography (DECT) in an ex vivo porcine plaque model,” *Physics in Medicine and Biology*, vol. 56, no. 22, pp. 7305–7316, 2011.

A Appendix

Table 1: Image acquisition parameters for the radiography samples. Images were acquired with thresholds every 0.5 keV within the energy threshold range. Lower and upper energy windows are those used for the radiography material decomposition. SD = source detector distance. SO = source object distance.

Sample	Energy threshold range [keV]	Lower energy window [keV]	Upper energy window [keV]	SD [cm]	SO [cm]	Exposure time [s]	Emission power [W]	Emission current [mA]	Acceleration voltage [V]	Focal spot size [μm]
Cu and Ag grids	4 - 10.5	7.5 - 9	9 - 10.5	55	10	30	15	214.3	70	10
Cu cable and Al foil	4 - 10.5	-	-	55	10	60	15	214.3	70	10
MultiHance	5 - 9.5	5.5 - 6	8 - 9.5	55	10	100	15	214.3	70	10
Plaque	4 - 9.5	-	-	55	10	40	15	214.3	70	10

Table 2: Image acquisition parameters for the CT samples. Lower and upper energy windows are those used for the CT material decomposition. SD = source detector distance. SO = source object distance.

Sample	Lower energy window [keV]	Upper energy window [keV]	Number of projections	Number of flat fields	SD [cm]	SO [cm]	Exposure time [s]	Emission power [W]	Emission current [mA]	Acceleration voltage [V]	Focal spot size [μm]
Cu cable and Al foil	7.5 - 9	9 - 10.5	720	5	55	10	100	15	214.3	70	10
MultiHance	4 - 6	8 - 9.5	720	5	55	15	150	15	214.3	70	10
Plaque	4 - 7	7.5 - 9	720	5	55	10	45	15	214.3	70	10